

Ram pressure stripping in elliptical galaxies: II. magnetic field effects

Min-Su Shin,^{1*} Mateusz Ruszkowski²

¹*Sub-department of Astrophysics, Department of Physics, University of Oxford, Keble Road, Oxford OX1 3RH*

²*Department of Astronomy, The University of Michigan, 500 Church Street, Ann Arbor, MI 48109, USA*

Accepted ... Received ...; in original form ..

ABSTRACT

We investigate the effects of magnetic fields and turbulence on ram pressure stripping in elliptical galaxies using ideal magnetohydrodynamics simulations. We consider weakly-magnetised interstellar medium (ISM) characterised by subsonic turbulence, and two orientations of the magnetic fields in the intracluster medium (ICM) – parallel and perpendicular to the direction of the galaxy motion through the ICM. While the stronger turbulence enhances the ram pressure stripping mass loss, the magnetic fields tend to suppress the stripping rates, and the suppression is stronger for parallel fields. However, the effect of magnetic fields on the mass stripping rate is mild. Nevertheless, the morphology of the stripping tails depends significantly on the direction of the ICM magnetic field. The effect of the magnetic field geometry on the tail morphology is much stronger than that of the level of the ISM turbulence. The tail has a highly collimated shape for parallel fields, while it has a sheet-like morphology in the plane of the ICM magnetic field for perpendicular fields. The magnetic field in the tail is amplified irrespectively of the orientation of the ICM field. More strongly magnetised regions in the ram pressure stripping tails are expected to have systematically higher metallicity due to the strong concentration of the stripped ISM than the less magnetised regions. Strong dependence of the morphology of the stripped ISM on the magnetic field could potentially be used to constrain the relative orientation of the ram pressure direction and the dominant component of the ICM magnetic field.

Key words: MHD – methods: numerical – galaxies: clusters: general – galaxies: evolution – galaxies: ISM – galaxies: intergalactic medium

1 INTRODUCTION

A number of environmental processes can alter galaxy evolution in cluster or group environments (Combes 2004; Boselli & Gavazzi 2006). Among these, ram pressure stripping process plays a particularly important role in galaxy evolution. This process strongly depends on galactic environment, and is especially strong when galaxies interact with high density ICM and move at large relative velocity with respect to the ICM. The impact of this process was first demonstrated comprehensively in a classic paper by Gunn & Gott (1972). Since then, a number of studies considered consequences of ram pressure stripping for galaxy evolution using numerical models. For example, these simulations considered a number of important issues such as: replenishment of the ISM lost from elliptical galaxies due to ram pressure stripping (Gaetz et al. 1987), possibility of

re-accretion of the stripped ISM (Balsara et al. 1994), complex time dependence of the ISM loss on the galaxy cluster environment (Stevens et al. 1999), inadequacy of analytical estimation for predicting the true ISM stripping rates (e.g. Roediger & Brüggén 2007), the effect of realistic ICM substructures on the ISM mass loss in cosmological setups (Tonnesen & Bryan 2008), impact of the orientation of disc galaxies with respect to their orbital trajectory (Jáchym et al. 2009), and star formation in the context of ram pressure stripping (Roediger et al. 2014).

As pointed out in Shin & Ruszkowski (2013, hereafter, Paper I), most simulations of ram pressure stripping did not include the effect of non-thermal energy components in the ISM and ICM. In the ISM, the non-thermal energy contributions include turbulent kinetic energy, magnetic fields, and cosmic-rays. In Paper I, we investigated the effect of the ISM turbulence on ram pressure stripping in elliptical galaxies, showing that the ISM mass loss is enhanced by including the ISM turbulence. Close et al. (2013) support our results

* E-mail: Min-Su.Shin@astro.ox.ac.uk, mateuszr@umich.edu

found in Paper I, using sub-grid turbulence models. However, our previous simulations ignored ISM and ICM magnetic fields, which are known to be present (Lesch & Bender 1990; Moss & Shukurov 1996; Widrow 2002; Vallée 2011; Arlen et al. 2012).

The process of ram pressure stripping in clusters or groups is to some extent analogous to the interaction of the heliosphere with the local magnetised ISM through which the Sun is moving. The ram pressure of the solar wind competes with that corresponding to the circum-heliospheric ISM, and prevents the ISM from completely blowing away the solar material (see Frisch et al. 2011, for a review). The geometry of the magnetic field in the local ISM and heliosphere, as well as the properties of turbulence, are not well understood. Nevertheless, the strength and geometry of the magnetic fields are thought to be important factors in regulating the mass exchange between the local ISM and heliosphere (Opher et al. 2009, 2011; Pogorelov et al. 2011).

The analogy between galactic ram pressure stripping and the interaction of the heliosphere with the local ISM suggests that the magnetic fields in the ISM and ICM should also affect the efficiency of the ram pressure stripping and the spatial distributions of the gas and magnetic fields. Ruszkowski et al. (2014) simulated ram pressure stripping in the case of a disk galaxy interacting with weakly magnetised ICM. They considered different orientations of the ICM magnetic fields and relative orientations of the disk with respect to the ram pressure direction. They find that the presence of magnetic fields has a strong effect on the tail morphology – it leads to filamentary tails rather than clumpy ones predicted by purely hydrodynamic simulations. In particular, their results show that the presence of magnetic fields may lead to the double tails similar to the ones seen in ESO 137-001 and ESO 137-002 (Sun et al. 2006, 2007; Zhang et al. 2013). Otmianowska-Mazur & Vollmer (2003) also studied the effects of magnetic fields on ram pressure stripping of late-type galaxies. However, their simulations did not include dynamical coupling of magnetic fields to the ISM and neglected ICM fields.

Since the magnetic field strength and its spatial distribution in elliptical galaxies are quite different from those representative of late-type galaxies, and because the distribution of the gas in late-type galaxies (relatively dense and flat gaseous disk and tenuous hot halo gas) is unlike what is seen in elliptical galaxies, the simulations of ram pressure stripping in disk galaxies cannot be used to understand the impact of the ram pressure stripping on elliptical galaxies.

In this second paper in the series, we aim to explore how the weakly-magnetised turbulent ISM and the magnetic field in the ICM affect the ram pressure stripping process in elliptical galaxies. We systematically investigate trends in mass stripping rates and morphology of the ram pressure stripping tails with the magnetic field strength, geometry, and ISM turbulence strength. While late-type galaxies have well-ordered large-scale structures in the spatial distribution of magnetic fields, early-type galaxies are expected to have highly tangled fields (see Beck 2011, for a review). In elliptical galaxies, the ISM pressure support against gravity is thought to come partially from subsonic turbulent motions (Werner et al. 2009; Ogrean et al. 2010; Sanders et al. 2011; de Plaa et al. 2012; Humphrey et al. 2013). Elliptical galaxies are also commonly found in the inner regions of

galaxy clusters, where the ICM is relatively dense. This hot ICM is thought to be weakly magnetised and turbulent (Taylor et al. 1994; Ge & Owen 1994; Govoni & Feretti 2004; Faltenbacher et al. 2005; Subramanian et al. 2006; Vacca et al. 2012a). The topology of the magnetic fields in the ICM is not known but some studies indicate that the fields can be coherent on the scales comparable to or larger than the size of an elliptical galaxy (e.g., Kuchar & Enßlin 2011; Vacca et al. 2012b). Therefore, it is necessary to incorporate the effects of the magnetised ICM and ISM in ram pressure stripping simulations of elliptical galaxies.

For the sake of simplicity, in this exploratory study we consider only very simplified geometry of the uniform ICM fields – parallel and perpendicular to the direction of the ram pressure. The objective of this investigation is to assess how sensitive the ram pressure stripping is to the field geometry in addition to the strength of the ISM turbulence. We focus on the effect of magnetic fields on the mass loss from galaxies and on the observable features of galaxies and their stripping tails. In future work, we will consider realistic distributions of the turbulent ICM magnetic fields, and the results presented here will help us to interpret future simulations. In order to highlight the differences between purely hydrodynamic simulations and MHD simulations, we compare main results presented here to those from our Paper I.

Our new simulations are complementary to the studies of cold fronts in clusters (e.g., Lyutikov 2006; Asai et al. 2007; Xiang et al. 2007; Dursi & Pfrommer 2008; Takizawa 2005). The physical scale and situation envisaged in our simulations are different. Ram pressure leads to the removal of the ISM from the galaxies, and the ICM is allowed to penetrate the galactic regions initially occupied by the ISM. In our simulations, the distributions of magnetic fields, temperature, and density are smooth on the boundary between the ISM and ICM, while most studies of the moving substructure in clusters assume a contact discontinuity or a sharp ISM/ICM boundary.

This paper is organised as follows. In Section 2, we discuss the simulation setup. Results are presented in Section 3. Finally, we discuss the implications of the results and conclude in Section 4. In the Appendix, we present the results of additional simulations to validate our main simulation.

2 SIMULATIONS

We use **FLASH4-alpha** code to solve ideal MHD equations (Fryxell et al. 2000; Lee & Deane 2009). We adopt unsplit MHD solver and use Roe Riemann solver with van Leer flux limiter. The initial distribution of the ISM is assumed to be spherical and in a hydrostatic equilibrium with static gravitational field of the galaxy. The stellar component of the gravitational field is described by a spherical Jaffe model. The dark matter distribution is chosen such that the total radial mass profile scales with radius r as r^{-2} (e.g., Ciotti et al. 2009a,b; Shin et al. 2010). We truncate the gravitational field beyond a truncation radius $R_t = 100$ kpc. This truncation approximates the effect of cluster tidal field on the galactic gravitational field (e.g., Limousin et al. 2009). The total stellar mass of the galaxy is about $10^{11} M_\odot$ and the mass of the dark matter halo is equal to the

stellar mass inside the stellar-mass effective radius 3 kpc (Deason et al. 2012). The centre of the galaxy is located at (0, 0, 0) and the simulation box covers a wide range from -320 to $+830$ kpc along x -axis, and from -256 to 256 kpc along other axes.

The density and temperature distributions of the ISM and ICM are continuous at R_t . The ICM density and temperature are constant and equal to 3×10^{-28} g cm $^{-3}$ and 2×10^7 K, respectively. The initial temperature distribution of the ISM is

$$T(r) = \begin{cases} T_i & \text{if } r < r_i \\ 2T_0/(1 + (r/r_0)^{-3}) & \text{otherwise,} \end{cases} \quad (1)$$

where $T_i = 8 \times 10^6$ K, $r_i = 50.9$ kpc, $T_0 = 1.3 \times 10^7$ K, and $r_0 = 66.6$ kpc. For the sake of simplicity, we assume the ideal gas equation of state for completely ionised gas with solar metallicity in both ISM and ICM.

Initially, both ISM and ICM include a weak magnetic field of 1.44×10^{-6} Gauss, which corresponds to plasma beta ($\beta = (nk_B T)/(B^2/(8\pi))$) of about 650 and 10 for the ISM at the galactic centre and ICM, respectively. Because $\beta \gg 1$, the initial density and temperature profiles do not depend on the strength of these initial fields. Since we also drive subsonic turbulence in the ISM, any small departures from perfect hydrostatic equilibrium due to magnetic forces are negligible compared to the departures from hydrostatic equilibrium due to driven subsonic turbulence in the ISM.

We consider two different directions of the magnetic field. In one set of simulations, the initial magnetic field is oriented along the x -axis, which is also the direction of the ram pressure. We call this set of simulations Case PA. The other set of simulations (Case PP) assumes the initial magnetic field along the y -axis.

As in Paper I, we use a modified stirring module in the FLASH code (Eswaran & Pope 1988; Fisher et al. 2008; Ruzkowski & Oh 2010). In order to generate weakly magnetised turbulent ISM, we perturb the initially hydrostatic ISM by adding kinetic energy to the gas at six different injection rates (see Table 1). The injection rates are per stirring mode. We use 152 modes corresponding to wavelengths ranging from 49 to 50 kpc. This stirring occurs only for $r < R_t$, and continues for the entire duration of the simulations. At 0.5 Gyr, the ICM of the constant density, temperature, and magnetic field starts to flow into the simulation domain from the $-x$ boundary and begins to exert ram pressure on the galaxy. At this time, the turbulence in the ISM has reached a steady state characterised by plasma β and velocity dispersions summarised in Table 1. At 0.5 Gyr, the ISM magnetic field in Case PA is weaker than in Case PP despite the fact that the same amount of kinetic energy is injected in both cases over the same amount of time. This happens because, during this initial stage, the boundary conditions are fixed in time are continuously reset at the $-x$ boundary. In Case PA, the magnetic field lines at the boundary are connected to the rest of the volume (at the boundary the fields are perpendicular to it) and, the fields are consequently not amplified as efficiently as in Case PP where the field lines do not intersect the $-x$ boundary. The magnetic field pressure is negligible compared to gas pressure in all runs initially. The simulations are evolved for 6 Gyr, including the initial 0.5 Gyr spent on stirring the ISM before the onset of the ICM inflow.

When investigating the effects of magnetic fields on ram pressure stripping, we compare Runs 0 and 2 of Case A in Paper I to Runs 0 and 3 of Cases PA and PP in this paper. Because the strength of turbulence in the ISM, which is measured by 1D RMS velocity dispersions, is very similar in these runs (see Table 1 in Paper I and Table 1 here), they are useful for isolating the effects of turbulence in the ISM.

Unless stated otherwise, we set the inflow velocity of the ICM at ~ 170 km/s, which is equal to Mach number of 0.25 with respect to the sound speed of the ICM. For Runs 0 and 5, we also investigate the effect of stronger ram pressure by increasing the speed of the ICM three times (i.e., by increasing the strength of the ram pressure nine times). These additional runs are denoted as Run 0h and Run 5h. Subsonic speeds may be typical of elliptical galaxies after they have been completely incorporated into galaxy clusters (e.g., Adami et al. 1998; Hwang & Lee 2008). We note that this may not be the case for both late-type galaxies and galaxies in the process of falling into clusters for the first time (e.g., Faltenbacher et al. 2005; Machacek et al. 2005, 2006).

We use two different kinds of tracers in the simulations – tracer particles and a passive scalar – in order to examine the mixing between the ISM and ICM, and to understand how the ISM is transported from the galaxy to the stripping tail. Passively moving particles are included with separate tags for the ISM and ICM. Including such particles allows us to track the origin of the particles and gas in the tail (Toschi & Bodenschatz 2009; Heath et al. 2007). We distribute 8,168 ISM particles uniformly inside R_t . We note that as the particles are dispersed through the volume, it is increasingly difficult to densely sample the growing tail volume with a finite number of particles. Therefore, we also introduce a passively advected scalar which we call “colour”. We use this quantity to estimate what fraction of mass in simulation cells comes from the ISM. If a cell contains only the ISM, the value of colour is, by definition, equal to 1. Colour does not allow us to track gas history. However, the distribution of colour shows how well two different kinds of gases are mixed (e.g., Shin et al. 2008).

We use the colour as a refinement variable. Because there is no absolute rule for the best variables of refinement and refinement conditions (Berger & Colella 1989; Li 2010, for discussion), we refine cells which have strong spatial variations of the colour above `refine_cutoff=0.8`, and derefine cells which have weak variations below `derefine_cutoff=0.2`, and use `refine_filter=10-2` in FLASH4-alpha¹. We use adaptive mesh refinement only for $r > R_t$. The refinement level is allowed to vary between 3 and 6 levels and the maximum resolution is 1 kpc. For $r < R_t$ we fix the spatial resolution at 2 kpc. We note that this refinement rule may affect structures found at $r > R_t$ quantitatively since it changes spatial resolution of the stripped ISM and the smallest scale of turbulent structures and magnetic-field amplification in that region. However, this configuration is the same as in our Paper I (i.e., pure hydro runs), allowing us to perform meaningful *relative* comparisons.

¹ See http://www.asci.uchicago.edu/site/flashcode/user_support/flash3_ug_3 for definitions of these simulation parameters.

Table 1. Simulation runs.

| Name | ISM injection energy ($\text{cm}^2 \text{s}^{-3}$) | Case PA | | Case PP | |
|-------|---|--------------------------------------|-------------------------|--------------------------------------|-------------------------|
| | | ISM 1D RMS velocity (Mach number) | $\langle \beta \rangle$ | ISM 1D RMS velocity (Mach number) | $\langle \beta \rangle$ |
| Run 0 | 2.5×10^{-8} | 0.022 | 44.8 | 0.023 | 24.0 |
| Run 1 | 2.5×10^{-7} | 0.028 | 53.2 | 0.027 | 28.2 |
| Run 2 | 5.0×10^{-7} | 0.036 | 45.4 | 0.033 | 25.8 |
| Run 3 | 1.0×10^{-6} | 0.047 | 35.3 | 0.042 | 25.4 |
| Run 4 | 2.0×10^{-6} | 0.060 | 30.8 | 0.055 | 28.0 |
| Run 5 | 4.0×10^{-6} | 0.084 | 34.5 | 0.078 | 33.0 |

ISM injection energy represents energy per stirring mode. ISM 1D RMS velocity is measured along the z -axis and is mass-weighted. $\langle \beta \rangle$ is a mass-weighted plasma beta parameter averaged inside R_t .

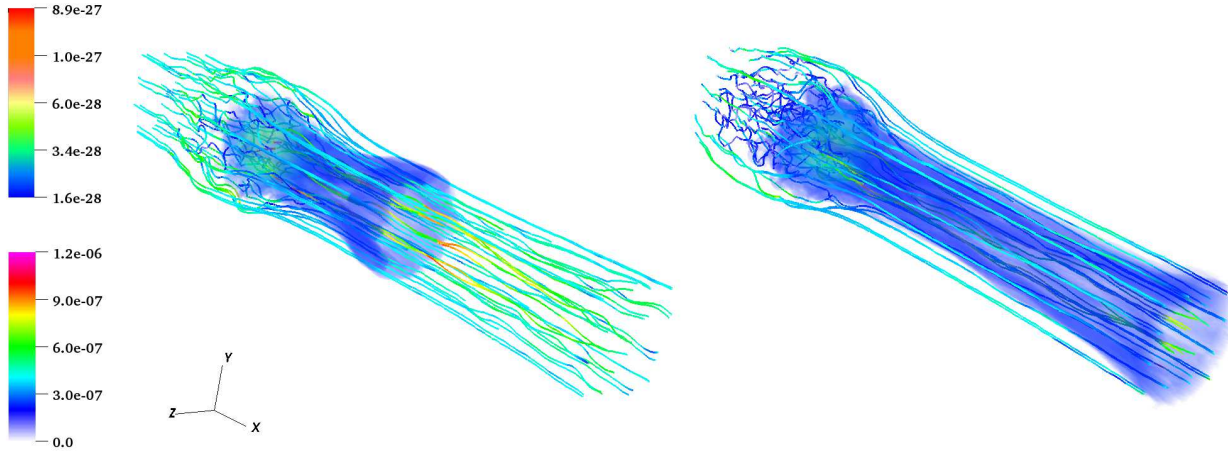


Figure 1. Gas density distributions for the ISM mass fractions above 1% and magnetic field magnitude in Run 5, Case PA at 3 (*left*) and 6 (*right*) Gyr. The top colour bar shows density in units of g cm^{-3} . The bottom colour bar shows magnetic field in $\sqrt{4\pi}$ Gauss. Therefore, 1 in this unit corresponds to $\sqrt{4\pi}$ Gauss. The magnetic field lines extend from about -320 to 650 kpc along x -axis.

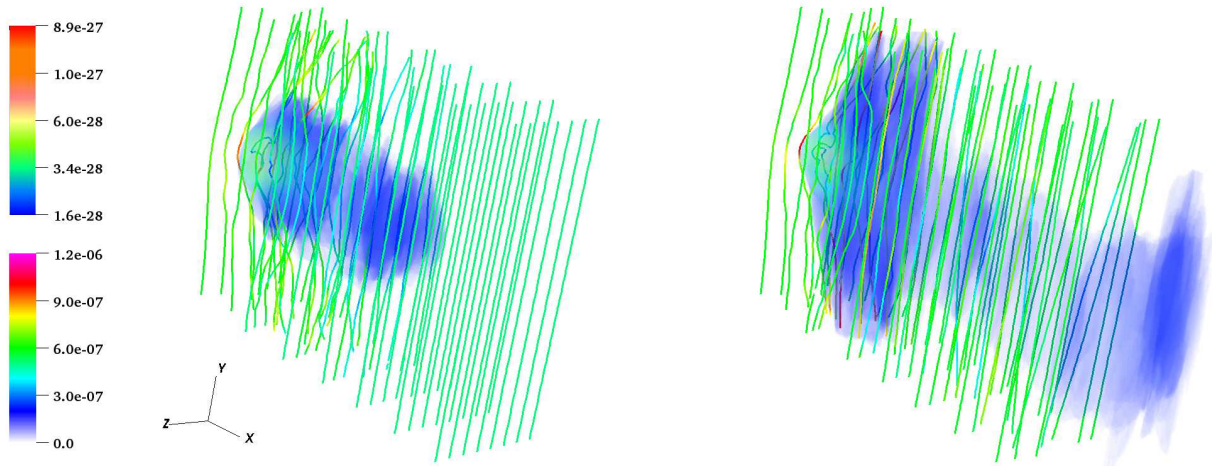


Figure 2. Same as Figure 1 but for Case PP. Significant magnetic field is found near the front side of the galaxy exposed to the inflowing ICM. The field is also amplified as it wraps around the galaxy. The direction of the tail is largely co-aligned with the magnetic field lines in the tail. The spatial scale is the same as in Figure 1. The field lines are plotted between -190 and 190 kpc along the y -axis.

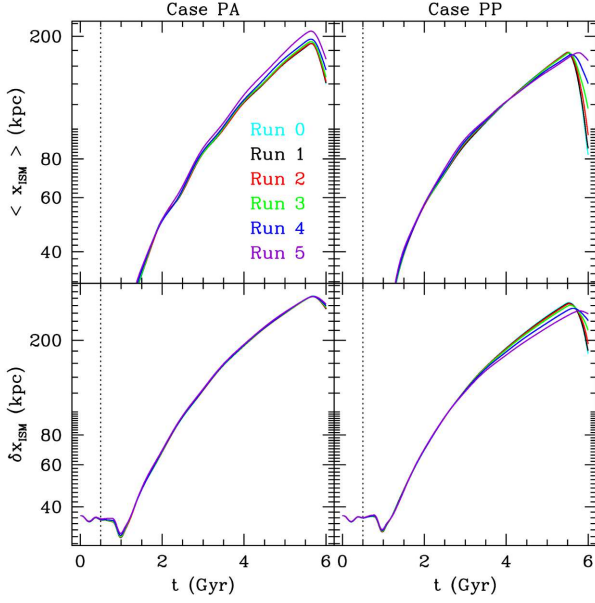


Figure 3. Evolution of $\langle x_{\text{ISM}} \rangle$ and δx_{ISM} in Cases PA (left) and PP (right). The dotted line corresponds to 0.5 Gyr when the ICM inflow begins to enter the simulation box. Around 1 Gyr, the ISM is strongly compressed by ram pressure, resulting in the decrease in δx_{ISM} . The tail is slightly less extended in Case PP than in Case PA.

3 RESULTS

We performed twelve simulations for the low-speed ICM velocity ~ 170 km/s and four runs for three times higher speeds. These simulations consider different ICM field orientations and turbulence strengths. We focus on the relative comparisons between these runs, but also examine the differences between purely hydrodynamical simulations presented in Paper I and the MHD simulations presented here.

3.1 Overall evolution

Figures 1 and 2 demonstrate that there are dramatic morphological differences in the gas distributions between Case PA and PP. Case PA simulation reveals a long tail stretched in the direction of the ram pressure, while Case PP produces a tail flattened in the $x - y$ plane, i.e., in the plane of the incoming ICM magnetic field. Magnetic fields are strongly amplified along the x -axis behind the galaxy in Case PA. On the other hand, in Case PP, the magnetic fields are amplified on the front side of the galaxy exposed to the incoming ICM. In this case, the ICM magnetic field bends along the sides of the galaxy and is amplified as it wraps around it. Strong magnetic fields are also produced as the flow converges behind the galaxy. While Case PA produces a flow converging from all directions in the $y - z$ plane, Case PP shows converging flow only along the z -axis, resulting in expansion along y -axis, i.e., along the direction of the ICM field.

The morphological differences between Case PA and PP are present even in the early phase of the evolution as shown in Figures 1 and 2. The initial stripping is effective in the outer regions of the galaxy. In Case PA, a ring-like structure

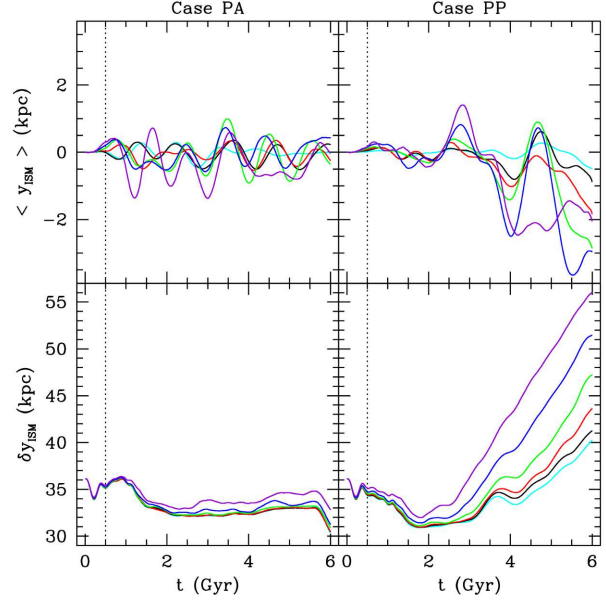


Figure 4. Evolution of $\langle y_{\text{ISM}} \rangle$ and δy_{ISM} in Cases PA (left) and PP (right). The colour coding of the different lines is the same as in Figure 3. In agreement with Figures 1 and 2, δy_{ISM} increases significantly in Case PP due to the expansion of the ISM along the direction of the ICM magnetic field. The run with the strongest turbulence (i.e., Run 5) shows the largest expansion along the y -axis.

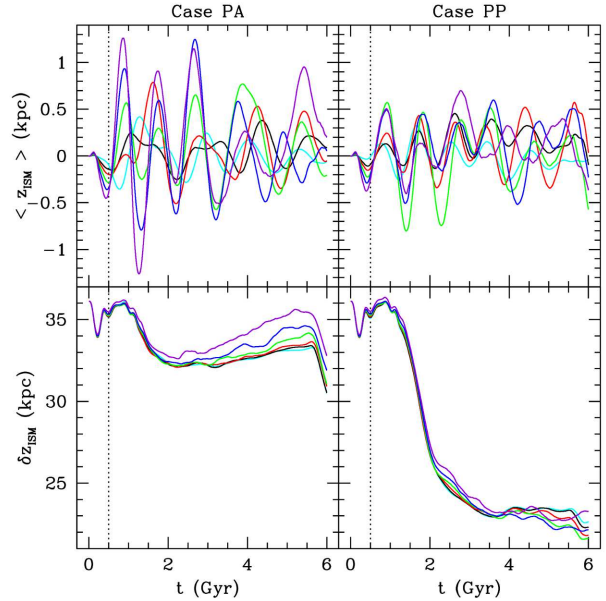


Figure 5. Evolution of $\langle z_{\text{ISM}} \rangle$ and δz_{ISM} in Cases PA (left) and PP (right). The colour coding of the different lines is the same as in Figure 3. In Case PP, as the stripped ISM converges behind the galaxy, δz_{ISM} becomes smaller than δy_{ISM} at a given time.

forms in the tip of the tail, which is predominantly made of the ISM stripped from the outer regions of the galaxy. On the other hand, in Case PP the morphology of the stripped ISM is sheet-like. The morphological differences grow significantly over time as more ISM is stripped from the galaxy. Unlike in Case PP, the tail morphology in Case PA more closely resembles that seen in purely hydrodynamical simulations presented in Paper I.

3.2 Spatial distribution of the ISM

We quantify the change in the morphology of the ISM by computing the mass-weighted average position and standard deviation of the ISM. For example,

$$\langle x_{\text{ISM}} \rangle = \frac{\sum_i C_i \rho_i V_i x_i}{\sum_i C_i \rho_i V_i}, \quad (2)$$

$$\delta x_{\text{ISM}} = \sqrt{\frac{\sum_i C_i \rho_i V_i (x_i - \langle x_{\text{ISM}} \rangle)^2}{\sum_i C_i \rho_i V_i}}, \quad (3)$$

where the index i represents a cell number, and ρ , V , C , and x , correspond to the density, cell volume, colour, and cell x -coordinates, respectively.

Since the ram pressure acts along the x -axis, we find the largest displacement of the ISM along that axis (see Figure 3). This figure also shows the initial compression of the gas around 1 Gyr when the ICM inflow first comes into contact with the ISM. The decrease in $\langle x_{\text{ISM}} \rangle$ and δx_{ISM} occurs around 5.5 Gyr because the ISM stripped in the early stage, i.e., the ring-like structure seen in Case PA, leaves the simulation box. In both Cases PA and PP, Run 3 leads to longer and wider stripping tail compared to the purely hydrodynamic case of Run 2 in Paper I. All of these runs have comparable turbulent gas velocity dispersions. We point out that the dependence of $\langle x_{\text{ISM}} \rangle$ and δx_{ISM} on the gas velocity dispersion is much weaker in the MHD runs compared to pure hydro runs presented in Paper I.

Figure 4 shows that the geometry of the ICM magnetic field strongly alters the spatial distribution of the stripped ISM along the y -axis. Differences appear even in the early phase of stripping. Around 1 Gyr, when the initial compression reduces δx_{ISM} in Case PA, δy_{ISM} increases slightly and shows a weak initial expansion along the direction perpendicular to the ram pressure direction. This weak expansion is not seen in Case PP. Instead, in Case PP we observe a decrease in δy_{ISM} up until 2 Gyr. This is caused by the stripping of the outer ISM. During this stage, the stripped ISM and the magnetic fields, that bend around the galaxy, are pushed closer to the x -axis, thus reducing δy_{ISM} . In Case PA, after 2 Gyr from the beginning of the simulation, the ISM in the tail does not change its width until around 5.5 Gyr, which marks the moment when the tail begins to escape the simulation box. On the other hand, in Case PP, the stripped ISM continues to spread along the y -axis after 2 Gyr.

The distribution of the gas along the z -axis presented in Figure 5 also reveals the impact of the ICM magnetic field. Because of the symmetry of the field in Case PA, the evolution of δz_{ISM} is similar to that of δy_{ISM} . In Case PP, as the stripped ISM flows behind the galaxy, the gas flow

converges along the z -axis. This results in the decrease in δz_{ISM} (see Figure 2).

The effects of different strength of the ISM turbulence, which is quantified in terms of the 1D RMS Mach number (see Table 1), are clearly seen in the evolution of δy_{ISM} in Case PP. However, in Case PA, $\langle x_{\text{ISM}} \rangle$, δy_{ISM} , and δz_{ISM} reveal only a weak dependence on the turbulence strength. As the turbulence strength increases, the tail becomes longer and wider in Case PA, but it expands only along y -axis in Case PP. The trends observed in Case PA are consistent with the conclusions from purely hydrodynamic simulations (see Figure 2 in Paper I).

3.3 Origin of the ISM in the tails

We trace the origin of the ISM in the stripping tail by examining the distributions of the passively moving ISM particles. These particles are initially distributed uniformly inside R_t . As the stirring process progresses, the ISM particles located initially in the galactic centre travel to outer regions of the galaxy due to random turbulent gas motions. These particles can be subsequently removed by ram pressure and transported to the tail.

Figure 6 shows the spatial distribution of the ISM particles in Case PA. While in the initial stages (at 2 Gyr) the stripping of particles originally located at $r > 70$ kpc is just as effective in Run 1 and 5, at 4.5 Gyr the distribution of particles on the distance versus initial distance plane becomes thicker, i.e., more ISM particles originate from initial distances $r > 50$ kpc, in Run 5 than Run 1. This difference is visible in Figure 6 where the effective area corresponding to the particle densities ranging from 1×10^{-3} to $5 \times 10^{-3} \text{ kpc}^{-2}$ is larger in Run 5 than in Run 1 for final distances greater than 100 kpc.

As shown in Figure 7, the tail in Case PP is weaker and consists of the ISM from a slightly narrower spatial range of initial distances than in Case PA. This difference is caused by less efficient stripping of the ISM originally located in the range $r > 60$ kpc in Case PP compared to Case PA. Even though Run 5 in Case PP shows turbulence-enhanced ISM loss over this spatial range when compared to Run 1 in Case PP, it still produces weaker tail than Run 5 in Case PA. This manifests itself as the difference in the spatial distribution of particle densities ranging from 1×10^{-3} to $5 \times 10^{-3} \text{ kpc}^{-2}$ in the distant parts of the tail.

We note that the differences between Case PA and PP are not due to turbulence strengths. Table 1 shows that the runs have very similar gas velocity dispersions in Cases PA and PP. Therefore, we attribute the differences in the morphology of the distributions shown in Figures 6 and 7 to the magnetic field configurations rather than turbulence strengths.

3.4 Evolution of the ISM mass retained in the galaxy

The decrease of the ISM mass as a function of time for different radial zones is shown in Figure 8. The largest amount of stripping is found in the runs with the strongest turbulence, i.e., Run 5. The galaxy in Case PA retains slightly larger amount of the ISM in the outer regions ($50 \lesssim r \lesssim 100$

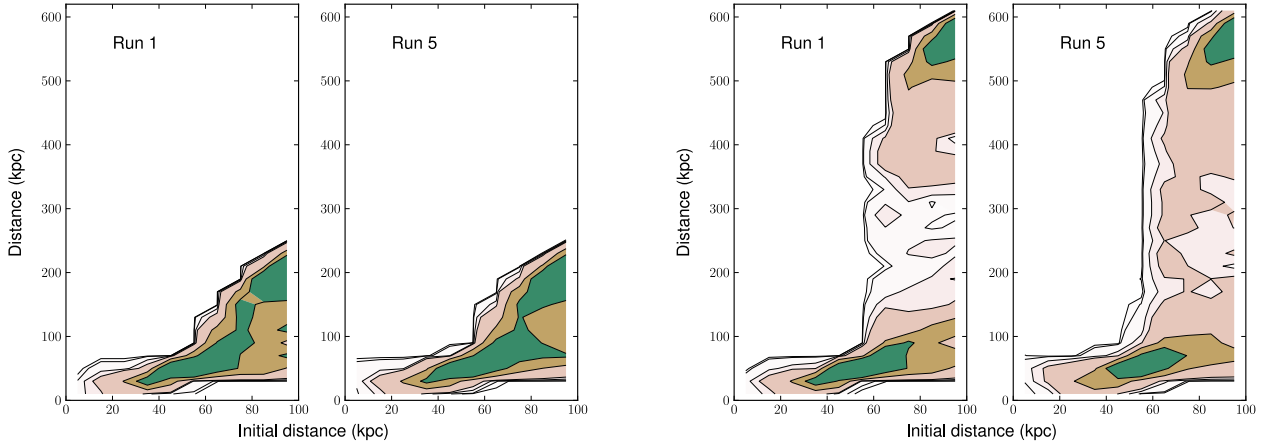


Figure 6. Density distribution of the passively moving ISM particles in Runs 1 and 5 at 2 (*left*) and 4.25 (*right*) Gyr in Case PA. The number density of the passive particles is measured on a uniform grid with bin sizes of 10 and 20 kpc for horizontal and vertical axes, respectively. The colour ranges correspond to bins defined by the number densities 5×10^{-5} , 1×10^{-4} , 5×10^{-4} , 1×10^{-3} , 5×10^{-3} , 1×10^{-2} , and $3.5 \times 10^{-2} \text{ kpc}^{-2}$. The distances of the particles are measured with respect to the galactic centre.

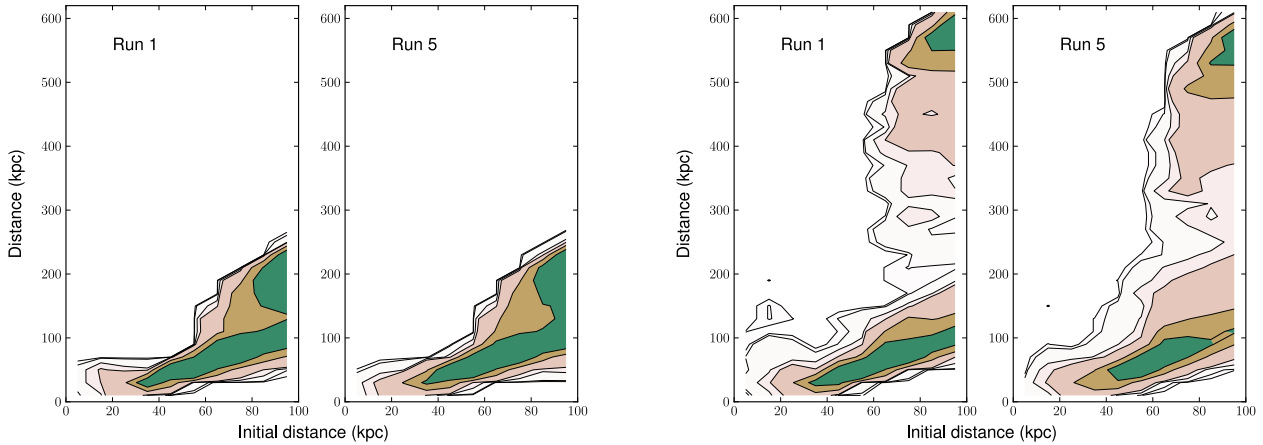


Figure 7. Density distributions of the passively moving ISM particles in Runs 1 and 5 at 2 (*left*) and 4.25 (*right*) Gyr for Case PP. The format of the plots is the same as in Figure 6.

kpc) than in Case PP. Efficient mixing leads to the loss of the ISM that was originally located in the centre ($r < 50$ kpc). Since this effect is weaker in Run 0, the galaxy in Run 0 retains about 11% more ISM than Run 5 at 6 Gyr in Case PA.

Considering only the effect of the magnetic fields on the ISM mass loss, we find that the magnetic field suppresses mass loss rates compared to the pure hydrodynamic cases. For example, at 6 Gyr the ISM mass remaining inside the galaxy in Run 3 is larger than that in a purely hydrodynamic simulation (i.e., Run 2 presented in Paper I). This choice of comparison runs is meaningful because we are comparing two different simulations characterised by a very similar level of the ISM turbulence as described by the magnitude of 1D RMS velocity dispersions (see Table 1 in Paper I and here). Specifically, in this example, in the MHD run of Case PA the galaxy retains 16% more ISM despite the fact that the

1D RMS velocity dispersion in that run is similar to that of the hydro Run 2 in Paper I.

The geometry of the ICM magnetic field also affects the efficiency of the ISM stripping. These differences are illustrated in Figure 8. For example, the galaxy in Run 1 in Case PA retains about 8% more ISM at 6 Gyr than Run 1 in Case PP despite the similar strength of turbulence in the beginning of the simulations although this difference in the ISM masses is only about 1% at 3 Gyr. The comparison of Run 5 results at 6 Gyr reveals that the galaxy in Case PA retains about 10% more ISM than in Case PP.

Considering the effects of both the magnetic field and the ISM turbulence together, we find that, irrespectively of the magnetic field orientation, the very presence of the magnetic field leads to a smaller spread in the ISM loss rates for a given spread in the 1D RMS velocity dispersion. For example, at 6 Gyr, in Run 0 of Case PP the galaxy retains about

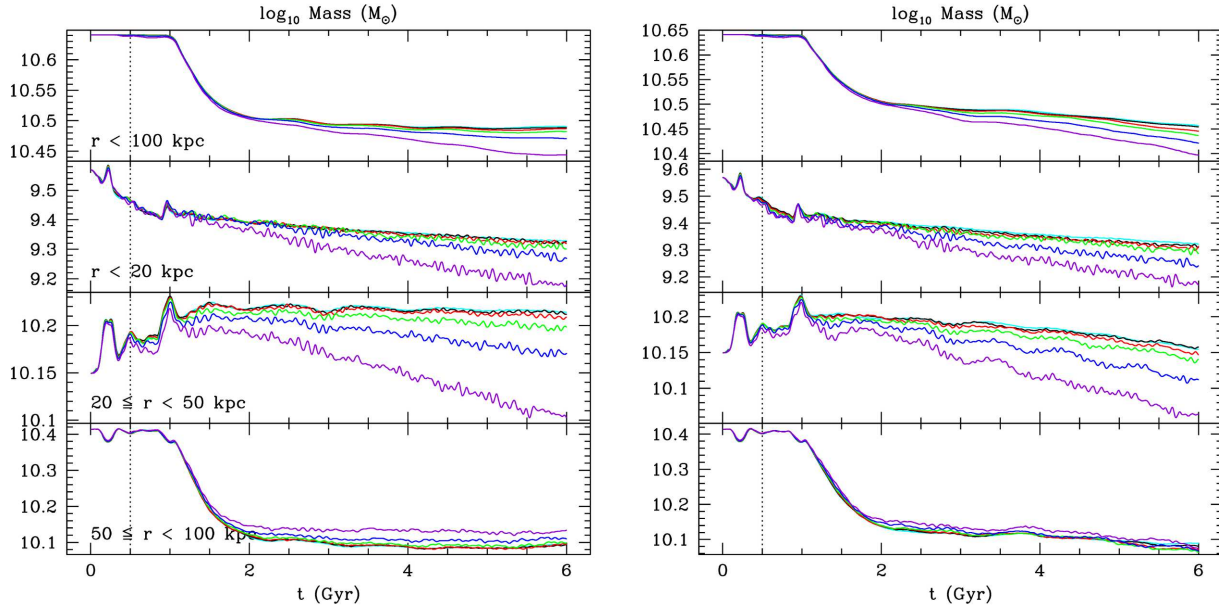


Figure 8. Evolution of the mass of intrinsic ISM in Case PA (*left*) and Case PP (*right*). From top to bottom, each panel shows the mass in four different radial zones: $r < 100$ kpc, $r < 20$ kpc, $20 \text{ kpc} \leq r < 50$ kpc, and $50 \text{ kpc} \leq r < 100$ kpc ($R_t = 100$ kpc). The colour coding of the different lines is the same as in Figure 3. The dotted vertical line corresponds to 0.5 Gyr when the ICM flow begins to enter the simulation box. Note that the vertical axis range is different in each panel.

15% more ISM than in Run 5. This difference is smaller than the one between Run 0 and Run 3 in the purely hydrodynamic case presented in Paper I, despite the fact that the gas velocity dispersions in this MHD case is even larger than that in the hydro case.

In summary, we find that increasing the level of turbulence in the ISM enhances the ISM loss. However, the strength of the ISM turbulence, as quantified by the 1D RMS velocity dispersion here, affects the ISM mass loss to lesser extent in the MHD simulations than in pure hydrodynamic ones. The geometry of the magnetic field in the ambient ICM alters the ISM loss rates.

3.5 Evolution of the total gas mass inside the galaxy

The inflowing ICM replaces the ISM inside R_t over time, and it blends with the ISM remaining in the galaxy. Figure 9 shows that the total gas mass inside R_t increases in both Case PA and PP early on ($t < 1$ Gyr), while the total amount of the ISM changes little (see Figure 8). This increase is mainly found in the outer region of the galaxy ($r < 50$ kpc). At later times, the total mass of the gas continuously decreases because the ICM is captured only temporarily in the outer region of the galaxy. Both the ISM and ICM are removed from the galaxy due to the combined action of turbulence, mixing, and ram pressure stripping. In analogy to the ISM mass stripping inside R_t , we find that more total mass is removed from the galaxy in Case PP than in Case PA.

As Figure 10 shows, we find that the relative change in the ISM mass is larger than the corresponding change in the total gas mass. This figure also shows that the variation in the retained ISM mass in Case PP is larger than in Case PA

despite the smaller difference of 1D RMS velocity dispersions between Runs 0 and 5 in Case PP than in Case PA (see Table 1). However, the total amount of gas inside R_t for different turbulence levels is very similar in Cases PA and PP.

Comparing hydrodynamics runs to MHD runs, both MHD Cases PA and PP exhibit less variation in the ISM mass and total gas mass with the ISM turbulence strength. For example, at 6 Gyr, the difference between Run 0 and 3 is about 2% in Case PA and 4% variations in Case PP (see Figure 10). Despite the fact that the difference in the ISM turbulence strength between Run 0 and 2 in the pure hydro case is very similar to that between Run 0 and 3 (either for Case PA or PP), the difference between the ISM mass remaining in the galaxy between Run 0 and 2 is about 6%, i.e., larger than in the MHD case described above. As far as the comparisons between the total gas mass are concerned, the comparison between the same pairs of simulations as above shows that the differences in the MHD cases are less than 0.5% for both Cases PA and PP, while the differences in the pure hydro cases are about 2% (see Figure 7 in Paper I). These comparisons prove that the strength of the ISM turbulence affects the ISM mass loss to lesser extent in the MHD simulations than in pure hydrodynamic ones.

In summary, strong ISM turbulence enhances mixing and mass loss. The effective total gas mass loss occurs despite the fact that the ICM replaces the ISM in the galaxy. This effective mass loss is possible because the ICM is incorporated into the galaxy only temporarily. However, the effect of turbulence has less impact on the stripping rates in the MHD simulations than in the hydrodynamic ones. When the ambient ICM magnetic field is perpendicular to the direction of the ram pressure (i.e., Case PP), the total gas mass decreases more rapidly than when the fields are parallel to the direction of ram pressure (i.e., Case PA).

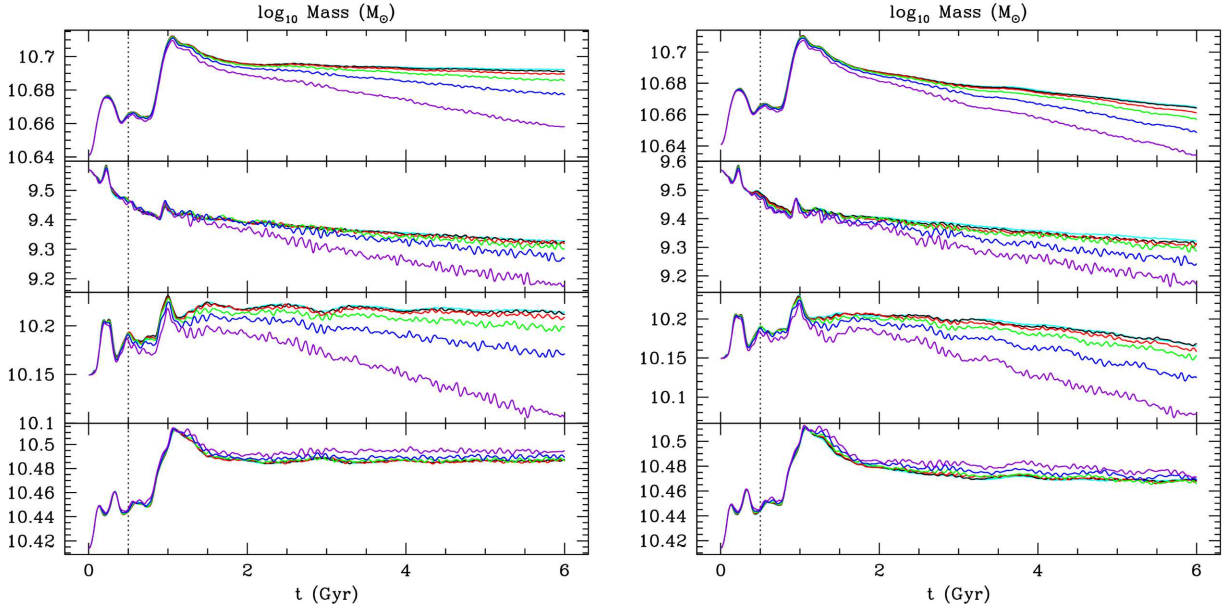


Figure 9. Mass evolution of the total gas mass inside R_t for Cases PA (*left*) and PP (*right*). From top to bottom, each panel shows the mass in four different radial zones: $r < 100$ kpc, $r < 20$ kpc, $20 \text{ kpc} \leq r < 50$ kpc, and $50 \text{ kpc} \leq r < 100$ kpc ($R_t = 100$ kpc). The dotted vertical line corresponds to 0.5 Gyr when the ICM starts to enter the simulation box. The colour coding of the different lines is the same as in Figure 3. Note that the ranges of the vertical axes are different in the left and right columns.

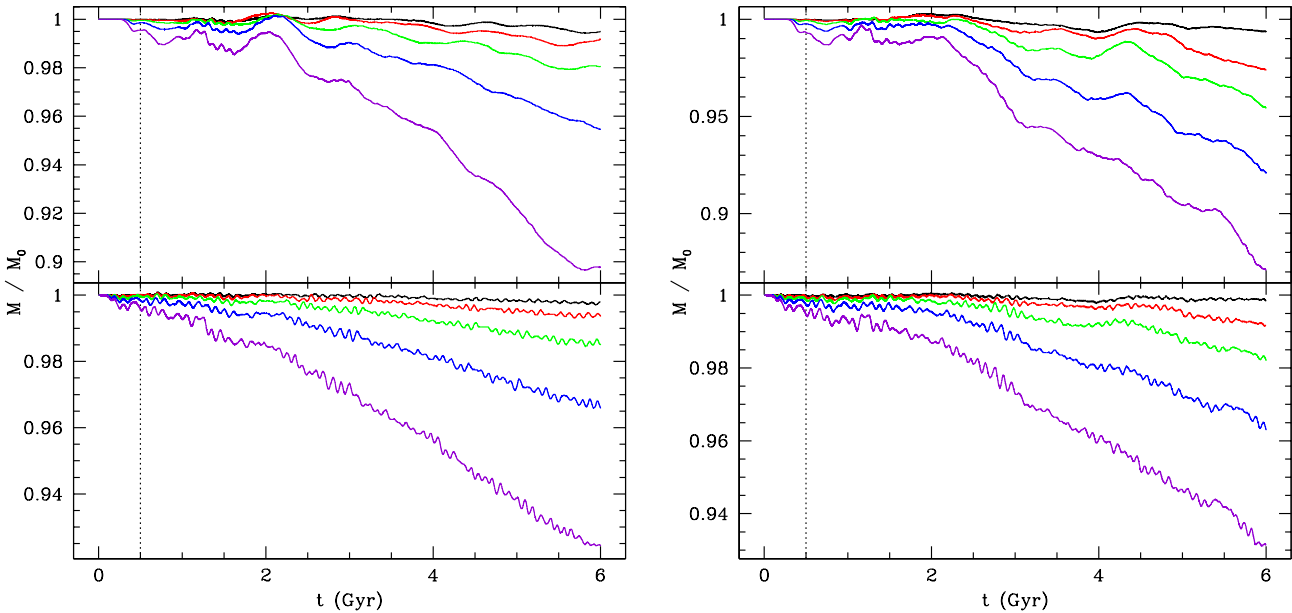


Figure 10. Evolution of the intrinsic ISM mass (*top*) and the total gas mass (*bottom*) inside R_t with respect to mass evolution of Run 0 in Cases PA (*left*) and PP (*right*). The colour scheme is the same as in Figure 3. The dotted vertical line corresponds to 0.5 Gyr when the ICM starts to flow into the simulation box.

3.6 Distribution of the magnetic fields

The differences in the evolution of the mass stripping in Cases PA and PP are closely related to the geometry of the magnetic field in these two cases. There is a marked difference between the magnetic field distributions in these two cases. Investigating the distribution of the magnetic field

in the galaxy and the stripping tail for simplified geometries of the external ICM magnetic fields is the first step that we need to take in order to correctly interpret the results of more sophisticated simulations with more realistic field topologies and make detailed predictions for observable quantities.

The most significant differences between Case PA and

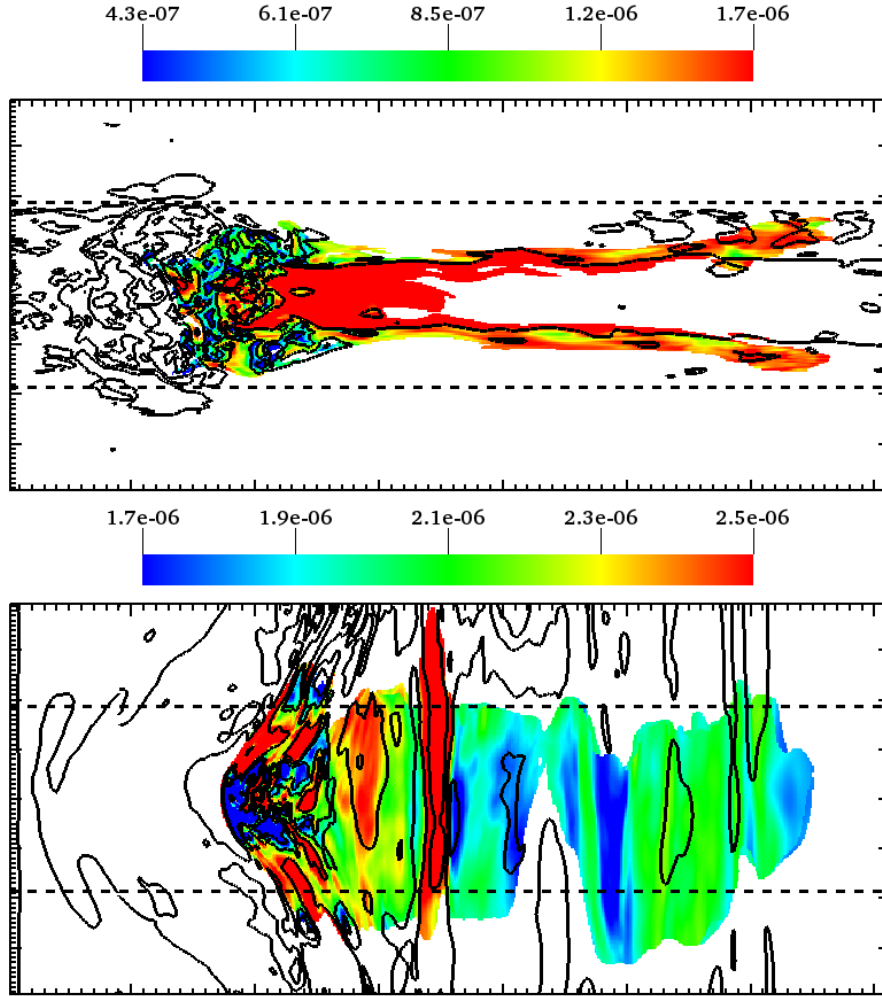


Figure 11. Cross-section through the magnetic-field magnitude distribution in Run 5 on $x - y$ plane centred on the galactic centre. The snapshot is taken at 5 Gyr. Results for Case PA are shown in the top panel and for Case PP in the bottom panel. Contour lines correspond to linearly-spaced values of the magnetic field magnitude ranging from 4.35×10^{-7} to 1.65×10^{-6} (G), and from 1.7×10^{-6} to 2.5×10^{-6} (G), in Cases PA and PP, respectively. The coloured regions represent areas with ISM density above 1% of total (i.e., ICM plus ISM) gas density. The unit of the colour bar is Gauss. The dashed lines correspond to 120 kpc from the galactic centre along the x -axis.

PP are seen in the distribution of strong magnetic field regions. As presented in Figure 11, the ICM converges behind the galaxy and is somewhat perturbed by the ISM turbulence in Case PA. Since the magnetic field coupled to the ISM is stretched behind the galaxy due to ram pressure, the spatial distribution of the strongly amplified magnetic field is coincident with that of the stripped ISM. Because the fields diverge in front of the galaxy, the side of the galaxy exposed to the incoming ICM flow has weaker magnetic fields than those in the tail where the gas flow converges. In Case PP, the stripped ISM forms structures flattened in the plane of the incoming ICM flow. The tail contains regions of amplified magnetic field. The origin of this amplification can be traced to the side of the galaxy exposed to the incoming ICM flow. It is there that the field perpendicular to the direction of the ram pressure is first compressed and amplified. This layer of amplified field is very thin compared to the size of the galaxy. The magnetic pressure in this layer is associated with more efficient ISM removal in Case PP

compared to Case PA. This amplified field is subsequently advected downstream and gives rise to the pockets of amplified magnetic field in the tail.

Figure 12 shows that the magnetic field in Case PA is relatively weak ($\sim 6 \times 10^{-7}$ Gauss) on the front side of the galaxy, i.e., for $x < -50$ kpc. This is consistent with Figure 11 discussed above. This effect is due to the divergence of the field in the inflowing ICM. This field is initially aligned with the direction of the ram pressure and begins to diverge as the ICM approaches the front of the galaxy. The field is stronger in the tail than in the front of the galaxy, and it is amplified to about 1.6×10^{-6} Gauss due to the converging flow past the galaxy.

In Case PP, the compressed ICM and ISM is associated with the amplification of the field in a thin layer in front of the galaxy. The field in this layer is dominated by the B_y component near $x \sim -50$ kpc as shown in Figure 12. The position of the maximum magnetic field strength gradually shifts in the downstream direction as the ICM penetrates

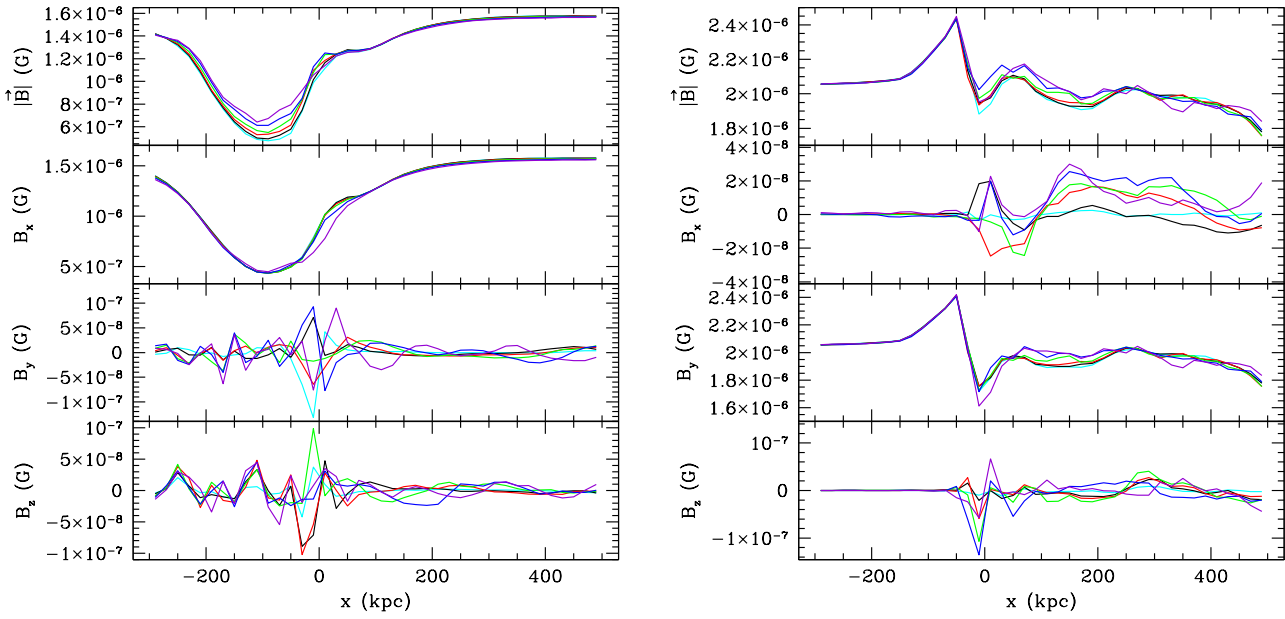


Figure 12. Mass-weighted magnetic field magnitude, x , y , and z -components of the magnetic field (from top to bottom) along the x -axis inside a cylinder of radius 120 kpc at 5 Gyr for Cases PA (left) and PP (right). The bin size along the x -axis is 20 kpc. The colour coding of the different lines is the same as in Figure 3.

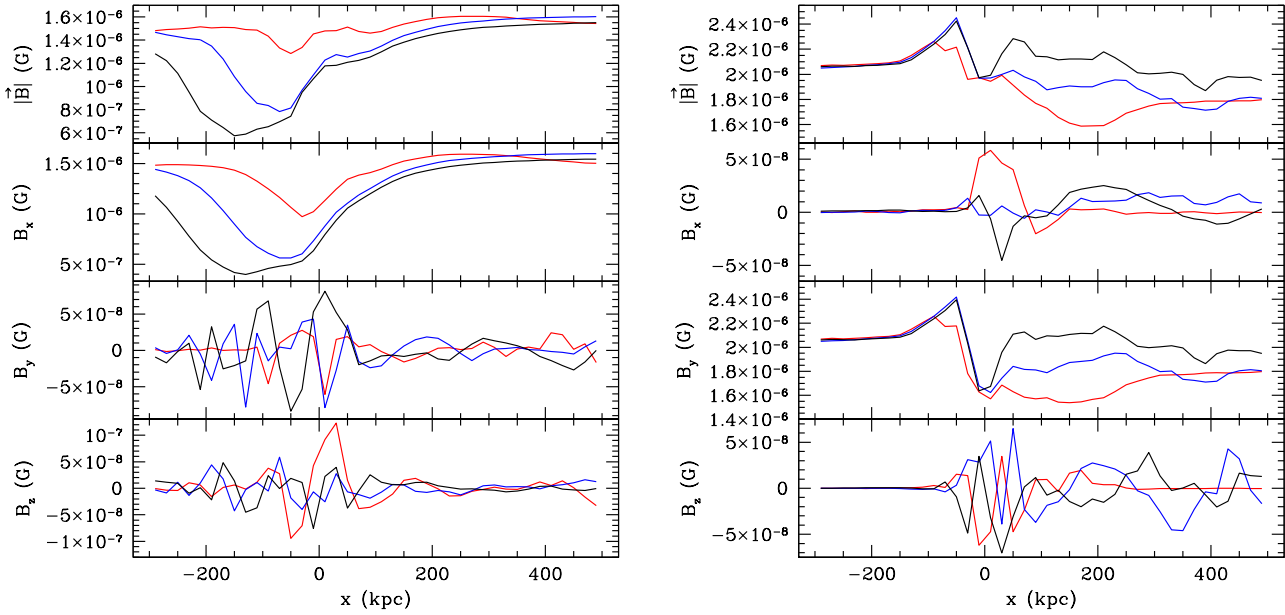


Figure 13. Mass-weighted magnetic field magnitude, x , y , and z -components of the magnetic field (from top to bottom) along the x -axis inside a cylinder with a radius 120 kpc in Run 5 for Cases PA (left) and PP (right) at 2 (red), 4 (blue), and 6 (black) Gyr. The bin size along the x -axis is 20 kpc.

further into the galaxy and the ISM is removed from it. In this case, the tail has a more strongly fluctuating magnetic field than the front side of the galaxy.

In Case PA, the decrease in the magnetic field strength around the front of the galaxy depends on the strength of turbulence (see Figure 12). Since strong turbulence in the

ISM enhances the ISM mass loss, one may expect that the magnitude of the magnetic field should decrease in the front of the galaxy (simply due to the removal of the magnetised gas from the galaxy). However, mixing of the ICM with the ISM, combined with continuous kinetic energy injection in the form of random motions in the galaxy, overcompensates

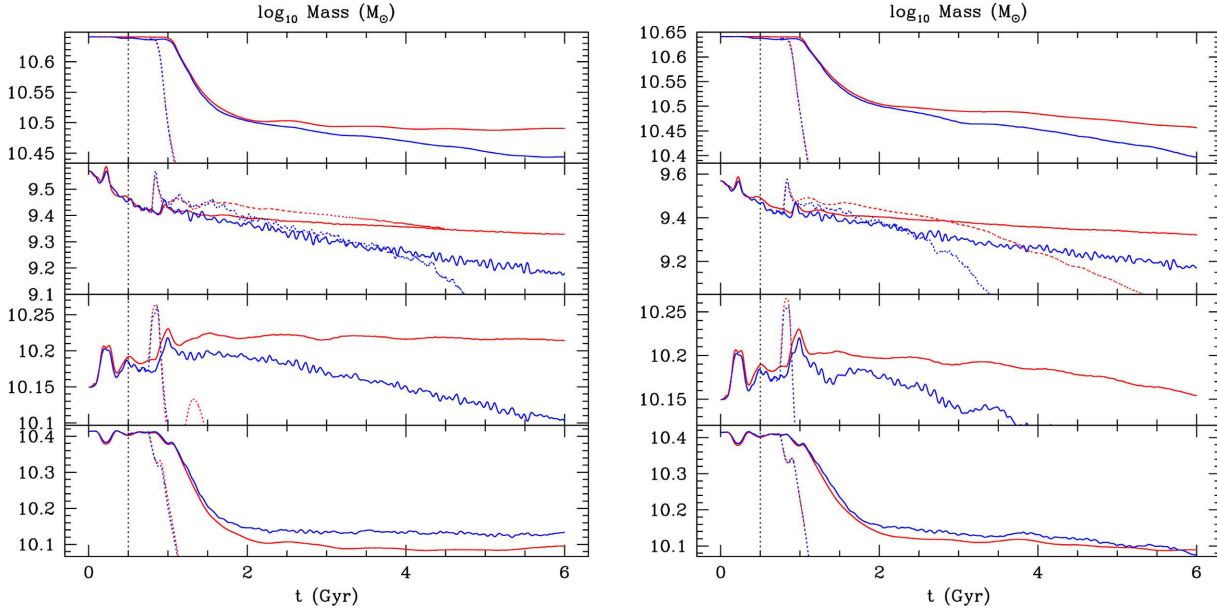


Figure 14. Mass evolution of the intrinsic ISM for Cases PA (*left*) and PP (*right*) in Runs 0h (*red*) and 5h (*blue*). From top to bottom, each panel shows the mass in four different radial zones: $r < 100$ kpc, $r < 20$ kpc, $20 \text{ kpc} \leq r < 50$ kpc, and $50 \text{ kpc} \leq r < 100$ kpc ($R_t = 100$ kpc). The solid lines correspond to Runs 0 and 5 and the dotted lines correspond to Runs 0h and 5h. The black dotted line corresponds to 0.5 Gyr when the ICM flow begins to enter the simulation box.

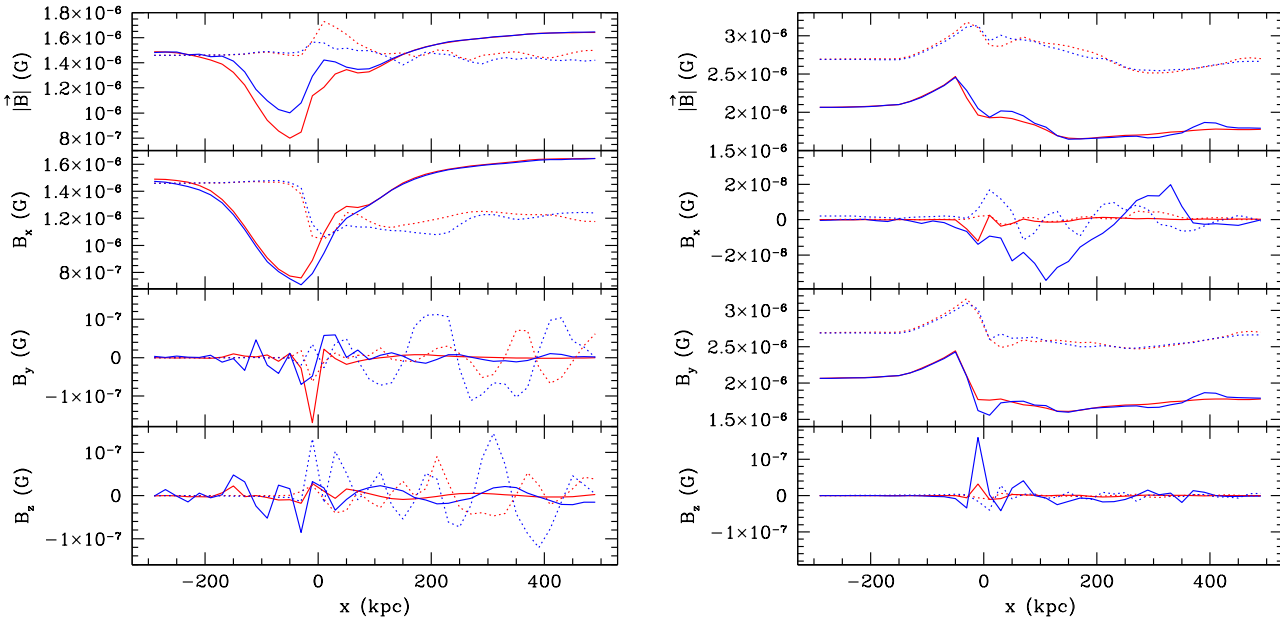


Figure 15. Mass-weighted x , y , and z components of the magnetic field (from top to bottom) along the x -axis inside a cylinder of radius 120 kpc at 3 Gyr for Cases PA (*left*) and PP (*right*). The bin size along the x -axis is 20 kpc. Colour coding and line styles are the same as in Figure 14.

for that loss of the magnetic energy inside R_t . For example, in Run 5, which is characterised by the strongest ISM turbulence, the magnitude of the magnetic field is slightly larger than in Run 0 on the front side of the galaxy.

In Case PP, at a given simulation time, the position of the strongest magnetic field does not vary as a function of the strength of the ISM turbulence. The location of the

magnetic field maximum is at $x \sim -50$ kpc, where the ram pressure is in approximate balance with the highly amplified magnetic and thermal pressures. The magnetic pressure is much larger than the thermal and turbulent pressures, and is dominated by the B_y component of the magnetic field. Since the speed of the ICM inflow is fixed, and its kinetic energy is the dominant form of energy, the amplified magnetic field

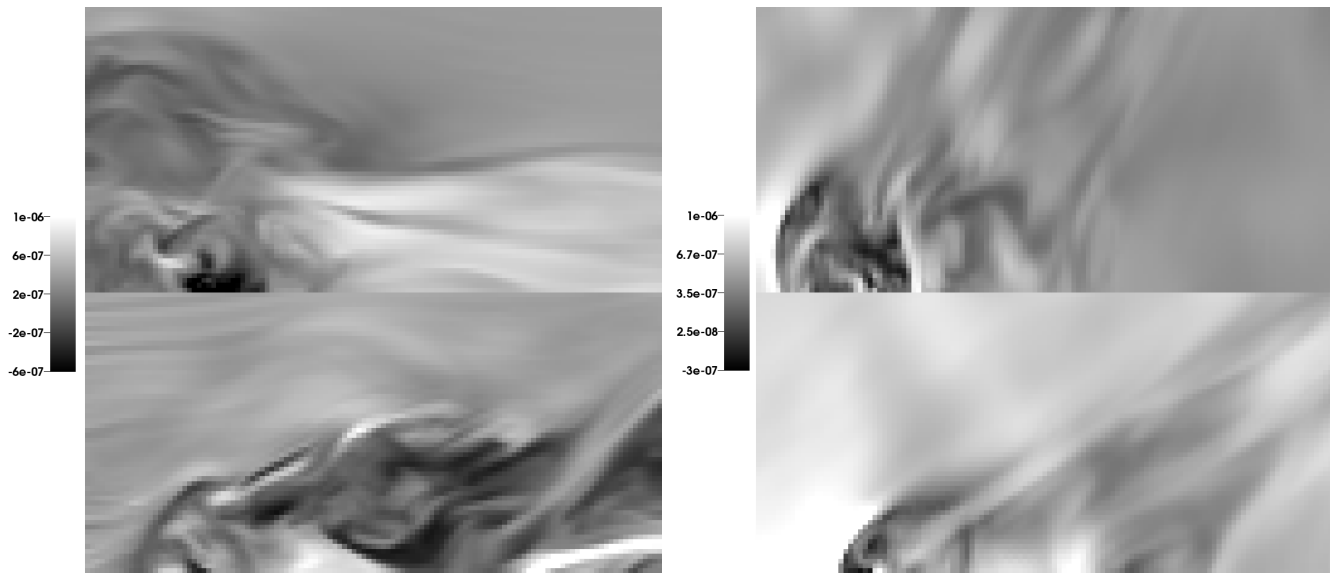


Figure 16. Distribution of B_x for Case PA and B_y for Case PP at 3 Gyr in the $x - y$ plane centred on the galactic centre. The size of each panel is -50 to 190 kpc along the x -axis and 0 to 120 kpc along the y -axis. The ordering of the panels is: Runs 5 (*top*), 5h (*bottom*), Cases PA (*left*), and PP (*right*). The unit of the colour bar is $\sqrt{4\pi}$ Gauss. Bright regions correspond to large positive values.

corresponds to the magnetic pressure limited by the fixed ram pressure. The position of the peak in the magnetic field strength does not change significantly once the magnetic field reaches its limiting value.

Figure 13 shows the evolution of the magnetic field distribution in Run 5. This figure sheds light on the origin of the differences between Case PA and PP shown in Figure 12. In Case PA, as the simulation continues, the continuous loss of the total gas in the front of the galaxy results in continuous decrease of the magnetic energy density. This is associated with continuous divergence of the magnetic fields on the front side of the galaxy. In Case PP, strong magnetic-field regions appear in the front of the galaxy. As the galaxy loses its total gas, the maximum position of the strong magnetic field moves closer to the galaxy toward $+x$ direction.

We now comment on the evolution of the magnetic field in the tails shown in Figure 13. In Case PA, the strong magnetic field in the tail is due to the convergence of the gas flow behind the galaxy. The strongest magnetic field in the tail corresponds to the gas that was stripped from the galaxy in the very early stages of the stripping process. The region of high amplification in the tail is continuously receding from the galaxy as also shown in Figure 11. Eventually, a part of the tail leaves the simulation box which leads to a small drop of the magnetic field magnitude at 6 Gyr (see the difference between the curves at 4 Gyr and 6 Gyr in Figure 13). In Case PP, as more ISM is transported to the tail and the ICM flow converges behind the galaxy, the average strength of the magnetic field in the tail increases. However, the collimation of the tail in Case PP is weaker than in Case PA since some of the stripped gas expands along the direction perpendicular to the wind direction (i.e., in the y -direction). The magnetic fields inside R_t remain relatively weak due to the continuous loss of gas from the galaxy. This explains the dip in the B_y component inside the galaxy and relatively strong fields in the downstream region behind the galaxy.

3.7 Stripping for higher ICM inflow velocity

It is not surprising that Runs 0h and 5h lead to stronger ISM mass loss than Runs 0 and 5. This difference is caused by nine times stronger ram pressure in Runs 0h and 5h. Figure 14 shows that in Runs 0h and 5h of both Cases PA and PP, the ISM mass inside R_t drops down to 70% of the original mass after about 0.5 Gyr of experiencing ram pressure stripping. This quick drop of the ISM mass is primarily driven by the change in the outer regions of the galaxy.

In Runs 0h and 5h for Cases PA and PP, the ram pressure completely dominates over magnetic fields and turbulence, and so the mass loss rate of the ISM is primarily determined by the strength of the ram pressure. Yet, the distributions of magnetic fields, presented in Figure 15 for Runs 0h and 5h, strongly depend on the geometry of magnetic fields – we observe strong differences between Case PA and PP. This conclusion is consistent with our previous results for lower-velocity ram pressure stripping, i.e., for Runs 0 and 5.

The distributions of B_x in Case PA and B_y in Case PP in Runs 0h and 5h bear some resemblance to the corresponding quantities in Runs 0 and 5. However, the compression of the magnetic fields in Runs 0h and 5h of Case PP is much stronger than in Runs 0 and 5. As shown in Figures 15 and 16, the peak in the magnetic field on the side of the galaxy exposed to the inflowing ICM is closer to the galaxy in Run 5h than in Run 5.

In Runs 0h and 5h of Case PA, the position of the lowest B_x appears closer to the galactic centre than in Runs 0 and 5. Due to the large inflow velocity, the point where the fields begin to diverge, and where the field strength is reduced, appears closer to the galaxy. Consequently, at distances $-50 < x < 0$ kpc the fields are stronger in Runs 0h and 5h than in Runs 0 and 5. In this case, the fast flow converging behind the galaxy generates eddies, resulting in a locally reversed flow direction and negative values of B_x .

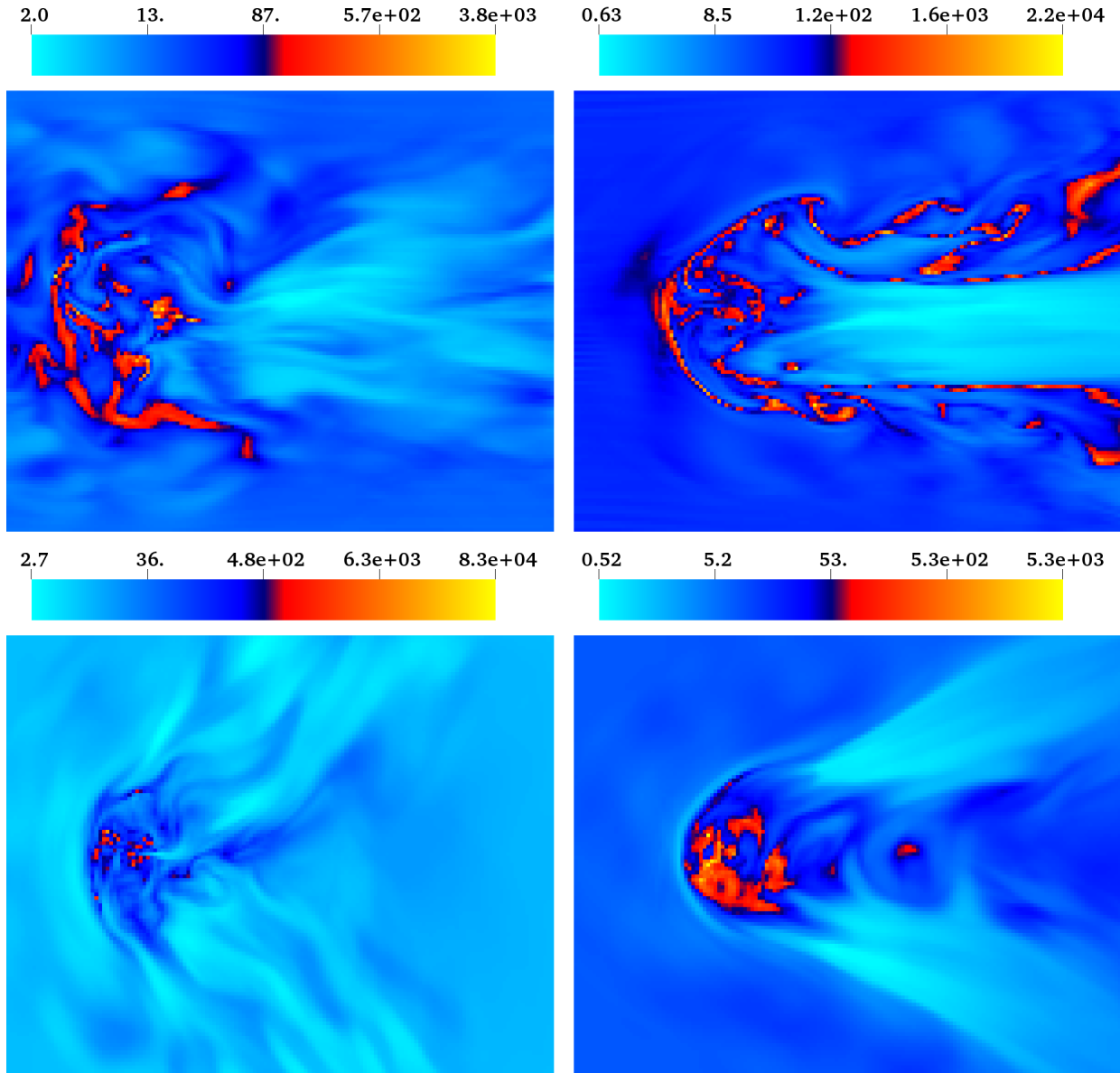


Figure 17. Distribution of the plasma beta parameter in the $x - y$ plane centred on the galactic centre. The size of each panel is -80 to 220 kpc along the x -axis and -120 to 120 kpc along the y -axis. The snapshots are taken at 1.5 Gyr. The ordering of the panels is: Runs 5 (left), 5h (right), Cases PA (top), and PP (bottom). Note that the colour bar ranges vary between panels. The ICM flows from the left to the right.

(see Figure 16). Therefore, the average B_x over $-20 < x$ kpc in Run 5h of Case PA is lower than in Run 5, but the average magnetic-field magnitude is higher in Run 5h than in Run 5.

In order to compare the dynamical impact of the amplified magnetic field in the runs with low and high ICM flow velocity, we show the distribution of the plasma beta in Runs 5 and 5h in Figure 17. In Case PA, the gas in the tails is characterised by low plasma beta. In those regions, the magnetic field is strong (see Figures 11 and 15). High plasma beta gas is distributed over the galaxy and the regions around the tail. High ram pressure leads to a strongly converging flow behind the galaxy and plasma beta is much

lower (~ 0.6) over a more coherent, narrower, and longer area in Run 5h than in Run 5.

Due to the fact that only B_y component in the ICM is present in Case PP, an extremely thin layer of low plasma beta appears on the front side of the galaxy in Run 5h as shown in Figure 17. Due to a relatively slower ICM flow, this feature is wider in Run 5 than Run 5h. In Run 5, the low plasma beta (~ 2.7) regions are distributed over a wide area on the side of the galaxy exposed to the ICM flow and in the region behind the galaxy. In Run 5h, following the expansion of the gas along the y -axis in front of the galaxy, the stripped ISM and magnetic field converge behind the galaxy. This results in the formation of the low plasma beta in a wing-like structure in the $x - y$ plane (see Figure 17).

Since high ram pressure creates a strongly converging flow behind the galaxy, the plasma beta is much lower (~ 0.5) over the more coherent area behind the galaxy in Run 5h than in Run 5.

In general, Runs 0h and 5h have a larger fraction of volume occupied by the gas characterised by lower plasma beta than Runs 0 and 5. Figure 17 shows that plasma beta reaches ~ 0.5 in Runs 0h and 5h and ~ 2 in Runs 0 and 5.

4 DISCUSSION AND CONCLUSIONS

We find that turbulence driven by continuous supply of kinetic energy to the ISM enhances the ISM mass loss in MHD simulations of ram pressure stripping. This effect is due to the mixing and efficient transport of the ISM to the outer regions of the galaxy. This conclusion is consistent with that found in Paper I which discusses ram pressure stripping in the context of purely hydrodynamic simulations. However, the effects of turbulence are weaker in the MHD case. We find that the ISM mass loss rate depends on the relative direction of the ICM magnetic field with respect to the ram pressure direction.

We show that the relative orientation of the magnetic field and the ram pressure direction is an important factor that determines the shape of the ISM stripping tails. This is shown in Figures 1, 2, and 11. When the ambient ICM has magnetic field components perpendicular to the ram pressure direction, the stripped ISM forms a wide tail with the stripped gas distributed in the plane of the incoming magnetic field. On the other hand, if the magnetic field is parallel to the ram pressure direction, a long and relatively narrow tail forms only along that direction, and the properties of the tail are similar to those found in pure hydrodynamic simulations.

We also demonstrate that the initial configuration of the fields affects the distribution of the magnetic field in the galaxy and the ram pressure stripping tail. When the ICM magnetic field is perpendicular to the ram pressure direction, the fields are compressed and wrapped/bent around the side of the galaxy exposed to the incoming ICM flow. When the ICM magnetic field is parallel to the ram pressure direction, the fields are weak on the side of the galaxy exposed to the wind, but strong magnetic fields can be found in the tail.

Radio observations of galaxies undergoing ram pressure stripping in the Virgo cluster have been used to investigate magnetic fields in the ICM around late-type galaxies and in their ISM (e.g., Weżgowiec et al. 2007; Chyży 2008; Vollmer et al. 2010; Pfrommer & Jonathan Dursi 2010). Although there are known ellipticals experiencing ram pressure stripping in the Virgo cluster, such as M86 (Randall et al. 2008) and NGC 4472 (Kraft et al. 2011), there are no reported magnetic field measurements in these cases yet.

As mentioned above, we demonstrate that the morphology of the tail and its magnetic field distribution is very sensitive to the relative direction of the ICM magnetic field with respect to the ram pressure direction. However, we stress that our current simulations do not imply that at any given time one is expected to see the whole length of the tails. Instead, our results show the history of the stripping process, and the regions which are close to the galaxy may best approximate instantaneous morphology of the galactic ISM

and stripping tail. However, if the magnetic field strength in these galaxies and in their tails could be measured, then such new observations could in principle help us to infer the relative angle between the ram pressure direction and the direction of the locally dominant magnetic field. However, the interpretation of such measurements will also require a new set of sophisticated simulations that include tangling of the magnetic field and turbulence in the ICM.

Figures 11, 12, and 13 show that, when the ICM field is perpendicular to the ram pressure direction, in the stripping tail we find thin layers of strong magnetic fields and a wing-like structure which is a filamentary region of enhanced magnetic fields approximately diagonal with respect to the leading edge of the galaxy in the $x - y$ plane. Since these structures contain some ISM due to ICM/ISM mixing and gas stripping (see Figure 11), and because the ISM is more metal-rich than the ICM (Humphrey & Buote 2006; Rasmussen & Ponman 2007; Anderson et al. 2009; Rasmussen & Ponman 2009; Ji et al. 2009; Million et al. 2011), our simulation results suggest a correlation between the magnetic field magnitude and the gas metallicity in the tail.

When the ICM magnetic field is parallel to the ram pressure direction, the regions of strong magnetic fields also correlate with the regions containing high ISM fractions, which again is due to the ICM-ISM mixing and gas stripping (see Figure 11). Therefore, the high-metallicity tail, which could be detected using X-ray from the hot gas or optical spectroscopy of HII regions (e.g., Rangarajan et al. 1995; Kim et al. 2008; Sun et al. 2010; Yoshida et al. 2012; Su et al. 2014), should be parallel to the direction of the ambient ICM magnetic field. On the other hand, the front side of the galaxy exposed to the ICM flow should be dominated by the ICM (i.e., by lower metallicity gas) characterised by relatively weak magnetic fields because the ICM penetrates the galaxy more easily and the field strength is reduced as the gas flow diverges in front of the galaxy and flows around it.

In summary, irrespectively of the direction of the ambient ICM fields, we expect that more strongly magnetised regions in the tails, which are dominated by the stripped ISM, will have systematically higher metallicity than less magnetised regions in the tails. This conclusion should not depend on the level of tangling of the ambient ICM field.

Our simulations show that ram pressure stripping can not only lead to the metal enrichment of the ICM (Schindler & Diaferio 2008), but provide the ICM with amplified magnetic fields (see also Arieli et al. (2011)). As shown in Figures 11 and 12, when the ICM magnetic fields are perpendicular to the ram pressure direction, parts of the stripping tail have ~ 1.2 times stronger magnetic field than the ICM in Run 5. Similarly, when the ICM field is parallel to the ram pressure direction, the magnetic field in the tail is about 15% higher than the ambient ICM field. These regions of the amplified magnetic field take the form of long coherent filaments and can extend to large distances from the galaxy (see Figure 11). Importantly, the magnetic field amplification increases for higher wind velocities. These stripped ISM magnetic fields may serve as localised seed fields for efficient field amplification due to other mechanisms such as the ICM turbulence (see Cho & Yoo 2012, for a discussion).

We show that the dependence of the ISM mass loss rate

on the magnetic field and turbulence strengths is insignificant when the ram pressure is much larger than the magnetic and turbulent pressures (see Figure 14). Therefore, if observations aim to explore the effects of the magnetic field and ISM turbulence on the ISM mass loss rate, then targets need to be cluster galaxies that move relatively slowly and experience a relatively low level of ram pressure. However, tail morphology depends sensitively on the geometry of the ICM magnetic fields irrespectively how fast/slow the galaxies are moving (see Figure 16).

There are multiple potentially important model components which could be investigated in future numerical simulations of ram pressure stripping. For example, our simulations only consider uniform fields in the ICM, while the realistic ICM is turbulent and the ICM fields are not uniform (Faltenbacher et al. 2005; Schekochihin & Cowley 2006; Subramanian et al. 2006; Mahdavi et al. 2008; Burns et al. 2010). Moreover, the density and velocity fluctuations in the ICM flow may also further complicate the stripping process. The ram pressure is proportional to the density and the square of galactic velocity with respect to the local ICM. Therefore, the stripping efficiency, tail morphology, and its magnetic fields may be affected by the ICM density and velocity fluctuations. The ICM turbulence can also alter the mixing between the stripped ISM and the ICM (da Silva et al. 2014).

We do not include realistic modelling of turbulence in the ISM. For example, in realistic systems, turbulence will be driven in part by supernovae and active galactic nuclei (AGN) (Mathews & Brighenti 2003; Elmegreen & Scalo 2004; Humphrey et al. 2013), which we do not explicitly include. Moreover, the interplay between turbulence and ram pressure stripping is further complicated by the possibility that ram pressure stripping itself could partially suppress star formation and AGN activities (e.g., Babul & Rees 1992; Murakami & Babul 1999; Kronberger et al. 2008; Shin et al. 2012). Such complexities are beyond the scope of the current paper.

Finally, in addition to the refinement methodology, other processes such as radiative cooling, heat conduction, and self-gravity of the gas can alter the mass loss rates, star formation in the stripping tail, and the morphology of the gas and magnetic field distributions (e.g. Asai et al. 2004a; Sivanandam et al. 2010; Yirak et al. 2010; Tonnesen & Bryan 2012; Boissier et al. 2012). In particular, heat conduction between the stripped warm ISM and the hot ICM might be an important process that shapes the tail morphology (Tribble 1989; Begelman & McKee 1990; Li et al. 2012). Since heat conduction is anisotropic in magnetised plasmas, including heat conduction can also affect cooling in the MHD case (e.g., Asai et al. 2004b; Orlando et al. 2008; Li et al. 2012).

ACKNOWLEDGEMENTS

We are grateful to Karen Yang and Dongwook Lee for useful discussions. We appreciate the input of an anonymous referee. MR acknowledges NSF grant AST 1008454 and NASA ATP 12-ATP12-0017. The software used in this work was in part developed by the DOE NNSA-ASC OASCR Flash Center at the University of Chicago. This work used the Extreme

Science and Engineering Discovery Environment (XSEDE), which is supported by National Science Foundation grant number OCI-1053575.

REFERENCES

- Adami C., Biviano A., Mazure A., 1998, *A&A*, 331, 439
 Anderson M. E. et al., 2009, *ApJ*, 698, 317
 Arieli Y., Rephaeli Y., Norman M. L., 2011, *ApJ*, 738, 15
 Arlen T. et al., 2012, *ApJ*, 757, 123
 Asai N., Fukuda N., Matsumoto R., 2004a, *ApJ*, 606, L105
 Asai N., Fukuda N., Matsumoto R., 2004b, *Journal of Korean Astronomical Society*, 37, 575
 Asai N., Fukuda N., Matsumoto R., 2007, *ApJ*, 663, 816
 Babul A., Rees M. J., 1992, *MNRAS*, 255, 346
 Balsara D., Livio M., O’Dea C. P., 1994, *ApJ*, 437, 83
 Beck R., 2011, in *American Institute of Physics Conference Series*, Vol. 1381, American Institute of Physics Conference Series, Aharonian F. A., Hofmann W., Rieger F. M., eds., pp. 117–136
 Begelman M. C., McKee C. F., 1990, *ApJ*, 358, 375
 Berger M. J., Colella P., 1989, *Journal of Computational Physics*, 82, 64
 Boissier S. et al., 2012, *A&A*, 545, A142
 Boselli A., Gavazzi G., 2006, *PASP*, 118, 517
 Burns J. O., Skillman S. W., O’Shea B. W., 2010, *ApJ*, 721, 1105
 Cho J., Yoo H., 2012, *ApJ*, 759, 91
 Chyży K. T., 2008, *A&A*, 482, 755
 Ciotti L., Morganti L., de Zeeuw P. T., 2009a, *MNRAS*, 393, 491
 Ciotti L., Ostriker J. P., Proga D., 2009b, *ApJ*, 699, 89
 Close J. L. et al., 2013, *MNRAS*, 436, 3021
 Combes F., 2004, in *IAU Symposium*, Vol. 217, *Recycling Intergalactic and Interstellar Matter*, P.-A. Duc, J. Braine, & E. Brinks, ed., p. 440
 da Silva C. B. et al., 2014, *Annual Review of Fluid Mechanics*, 46, 567
 de Plaa J. et al., 2012, *A&A*, 539, A34
 Deason A. J. et al., 2012, *ApJ*, 748, 2
 Dursi L. J., Pfrommer C., 2008, *ApJ*, 677, 993
 Elmegreen B. G., Scalo J., 2004, *ARA&A*, 42, 211
 Eswaran V., Pope S. B., 1988, *Computers and Fluids*, 16, 257
 Faltenbacher A. et al., 2005, *MNRAS*, 358, 139
 Fisher R. T. et al., 2008, *IBM Journal of Research and Development*, 52, 127
 Frisch P. C., Redfield S., Slavin J. D., 2011, *ARA&A*, 49, 237
 Fryxell B. et al., 2000, *ApJS*, 131, 273
 Gaetz T. J., Salpeter E. E., Shaviv G., 1987, *ApJ*, 316, 530
 Ge J., Owen F. N., 1994, *AJ*, 108, 1523
 Govoni F., Feretti L., 2004, *International Journal of Modern Physics D*, 13, 1549
 Gunn J. E., Gott, III J. R., 1972, *ApJ*, 176, 1
 Heath D., Krause M., Alexander P., 2007, *MNRAS*, 374, 787
 Humphrey P. J., Buote D. A., 2006, *ApJ*, 639, 136
 Humphrey P. J. et al., 2013, *MNRAS*, 430, 1516
 Hwang H. S., Lee M. G., 2008, *ApJ*, 676, 218
 Jáchym P. et al., 2009, *A&A*, 500, 693

- Ji J. et al., 2009, *ApJ*, 696, 2252
 Kim D.-W. et al., 2008, *ApJ*, 688, 931
 Kraft R. P. et al., 2011, *ApJ*, 727, 41
 Kronberger T. et al., 2008, *A&A*, 481, 337
 Kuchar P., Enßlin T. A., 2011, *A&A*, 529, A13
 Lee D., Deane A. E., 2009, *Journal of Computational Physics*, 228, 952
 Lesch H., Bender R., 1990, *A&A*, 233, 417
 Li S., 2010, *Journal of Computational and Applied Mathematics*, 233, 3139
 Li S., Frank A., Blackman E., 2012, *ApJ*, 748, 24
 Limousin M. et al., 2009, *ApJ*, 696, 1771
 Lyutikov M., 2006, *MNRAS*, 373, 73
 Machacek M. et al., 2005, *ApJ*, 621, 663
 Machacek M. et al., 2006, *ApJ*, 644, 155
 Mahdavi A. et al., 2008, *MNRAS*, 384, 1567
 Mathews W. G., Brighenti F., 2003, *ARA&A*, 41, 191
 Million E. T. et al., 2011, *MNRAS*, 418, 2744
 Moss D., Shukurov A., 1996, *MNRAS*, 279, 229
 Murakami I., Babul A., 1999, *MNRAS*, 309, 161
 Ogreaan G. A. et al., 2010, *MNRAS*, 406, 354
 Opher M. et al., 2009, *Nature*, 462, 1036
 Opher M. et al., 2011, *ApJ*, 734, 71
 Orlando S. et al., 2008, *ApJ*, 678, 274
 Otmianowska-Mazur K., Vollmer B., 2003, *A&A*, 402, 879
 Pfrommer C., Jonathan Dursi L., 2010, *Nature Physics*, 6, 520
 Pogorelov N. V. et al., 2011, *ApJ*, 742, 104
 Randall S. et al., 2008, *ApJ*, 688, 208
 Rangarajan F. V. N. et al., 1995, *MNRAS*, 277, 1047
 Rasmussen J., Ponman T. J., 2007, *MNRAS*, 380, 1554
 Rasmussen J., Ponman T. J., 2009, *MNRAS*, 399, 239
 Roediger E., Brügggen M., 2007, *MNRAS*, 380, 1399
 Roediger E. et al., 2014, *MNRAS*, 443, L114
 Ruszkowski M. et al., 2014, *ApJ*, 784, 75
 Ruszkowski M., Oh S. P., 2010, *ApJ*, 713, 1332
 Sanders J. S., Fabian A. C., Smith R. K., 2011, *MNRAS*, 410, 1797
 Schekochihin A. A., Cowley S. C., 2006, *Physics of Plasmas*, 13, 056501
 Schindler S., Diaferio A., 2008, *Space Sci. Rev.*, 134, 363
 Shin M.-S., Ostriker J. P., Ciotti L., 2010, *ApJ*, 711, 268
 Shin M.-S., Ostriker J. P., Ciotti L., 2012, *ApJ*, 745, 13
 Shin M.-S., Ruszkowski M., 2013, *MNRAS*, 428, 804
 Shin M.-S., Stone J. M., Snyder G. F., 2008, *ApJ*, 680, 336
 Sivanandam S., Rieke M. J., Rieke G. H., 2010, *ApJ*, 717, 147
 Stevens I. R., Acreman D. M., Ponman T. J., 1999, *MNRAS*, 310, 663
 Su Y. et al., 2014, *ApJ*, 786, 152
 Subramanian K., Shukurov A., Haugen N. E. L., 2006, *MNRAS*, 366, 1437
 Sun M. et al., 2010, *ApJ*, 708, 946
 Sun M., Donahue M., Voit G. M., 2007, *ApJ*, 671, 190
 Sun M. et al., 2006, *ApJ*, 637, L81
 Takizawa M., 2005, *ApJ*, 629, 791
 Taylor G. B., Barton E. J., Ge J., 1994, *AJ*, 107, 1942
 Tonnesen S., Bryan G. L., 2008, *ApJ*, 684, L9
 Tonnesen S., Bryan G. L., 2012, *MNRAS*, 422, 1609
 Toschi F., Bodenschatz E., 2009, *Annual Review of Fluid Mechanics*, 41, 375
 Tribble P. C., 1989, *MNRAS*, 238, 1247
 Vacca V. et al., 2012a, *A&A*, 540, A38
 Vacca V. et al., 2012b, *A&A*, 540, A38
 Vallée J. P., 2011, *New A Rev.*, 55, 91
 Vollmer B. et al., 2010, *A&A*, 512, A36
 Werner N. et al., 2009, *MNRAS*, 398, 23
 Weźgowiec M. et al., 2007, *A&A*, 471, 93
 Widrow L. M., 2002, *Reviews of Modern Physics*, 74, 775
 Xiang F. et al., 2007, *MNRAS*, 379, 1325
 Yirak K., Frank A., Cunningham A. J., 2010, *ApJ*, 722, 412
 Yoshida M. et al., 2012, *ApJ*, 749, 43
 Zhang B. et al., 2013, *ApJ*, 777, 122

APPENDIX A: INITIAL MAGNETIC FIELDS IN THE WEAK RAM PRESSURE STRIPPING CASE

We present results for different strengths of the initial magnetic fields in the computational domain and at the inflow boundary. The fields are initially constant in the whole computational domain and constant throughout the simulation at the inflow boundary. The evolution of the fields that enter the simulation box in Cases PA and PP is different in these two cases in part because the field strength applied at the boundary transforms differently depending on the relative angle of the magnetic field with respect to the inflow direction.

The impact of different field orientations on the field entering the simulation domain is shown in Figures 12 and 13. In particular, Figure 13 shows that the magnitude of the magnetic field entering the simulation box is about 1.44×10^{-6} Gauss in Case PA and about 2.04×10^{-6} Gauss in Case PP. This difference occurs despite the fact that, in both cases, we assume that the initial ISM/ICM magnetic field strengths and the strength of the field at the boundary are all identical (i.e., 1.44×10^{-6} Gauss).

In order to eliminate these differences in the level of the field entering the computational box, we perform Case PA runs with a stronger magnetic field and use 2.04×10^{-6} Gauss instead of the original magnitude of 1.44×10^{-6} Gauss. As in the original runs, we initialise the same magnetic field in both the ISM and ICM (this time 2.04×10^{-6} Gauss), keeping all other parameters unchanged. In these new Case PA runs, the effective strength of the field that initially enters the computational domain approximately matches that in the original run in Case PP. Thus, these new runs allow us to isolate the effects of the geometry of the initial/inflowing fields on the amount of gas stripping and the strength of the resulting magnetic field.

Figure A1 shows the distribution of the evolved field in the new runs. Although the general trends seen in the new runs are not different from those found in the original runs, the new runs demonstrate that the stronger initial and boundary magnetic fields lead to generally stronger magnetic fields (including in the regions directly in front of the galaxy). However, as the dynamical effects of the magnetic field are now stronger than in the original runs, the buildup of the field just ahead of the galaxy affects the field at a larger upstream distance away from the galaxy. This results in lower fields in that region compared to the original run.

Figure A2 shows that the stronger field in the new runs

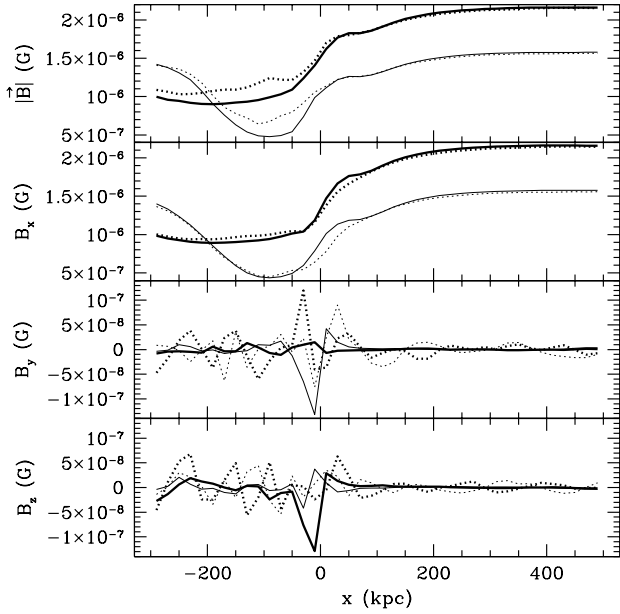


Figure A1. Mass-weighted average magnetic field magnitude, x , y , and z -components (from top to bottom) along x -axis for Case PA. The magnitudes are measured inside a cylinder of radius 120 kpc in radius at 5 Gyr. The original runs are shown as *thin lines* and the new runs as *thick lines*. The results are presented for Runs 0 (*solid line*) and 5 (*dotted line*). The bin size along x -axis is 20 kpc.

results in more efficient removal of the ISM beyond R_t compared to that seen in the original runs. The figure also compares the evolution of the total gas mass in the galaxy between the new and old runs. While the differences between the values of the total mass inside R_t are not significant in Run 0, the stripping is less efficient for stronger fields in Run 5 (i.e., when turbulence is stronger). However, the difference between Run 0 and 5 is smaller in the new runs than in the original runs because the impact of different turbulence strength is overwhelmed by the effect of the magnetic field (which is stronger in the new runs).

The new runs also allow us to check if the large loss of the ISM found in Case PP is solely caused by the differences between the magnetic field strengths in the inflowing ICM in Cases PA and PP. For example, the mass of the ISM retained inside R_t in the new Run 5 of Case PA is about $10^{10.43} M_\odot$ at 6 Gyr, which is about 7% more than in Case PP (see Figure A2 and Figure 8). This difference is quite similar to the one between Case PP and PA in the original runs. Since the strength of the inflowing fields (and the initial ones) in the original Case PP and the new Case PA is now very similar, the differences in the ISM stripping rates can now be attributed to the geometry of the magnetic field rather than the field strengths. Similar conclusions can be drawn with regard to the total gas stripping. Specifically, Figure A2 shows that the removal of the total gas from within $r < R_t$ is somewhat more efficiently suppressed due to deeper penetration of the ICM into the galaxy in the new Case PA compared to the original Case PP (see Figure 9). Therefore, the differences between the original Case PP and the new

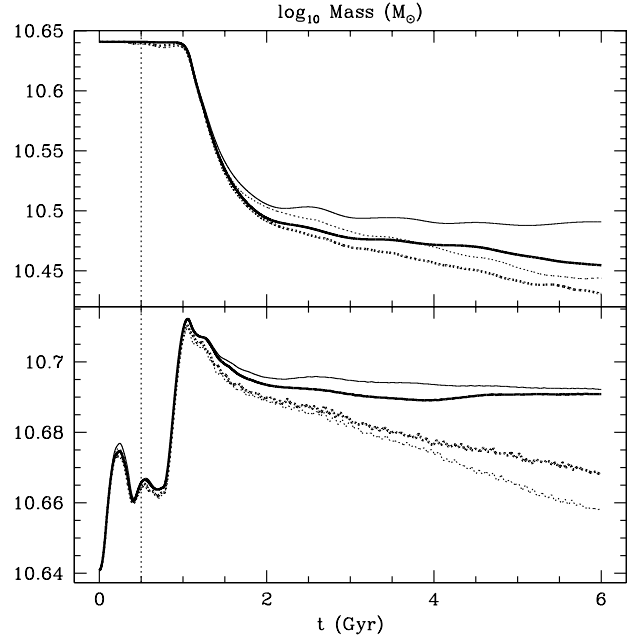


Figure A2. Mass evolution of the intrinsic ISM mass (*top*) and the total gas mass (*bottom*) inside R_t in Case PA. With the exception of the vertical dotted line that corresponds to 0.5 Gyr when the ICM begins to flow into simulation box, all line styles have the same meaning as in A1.

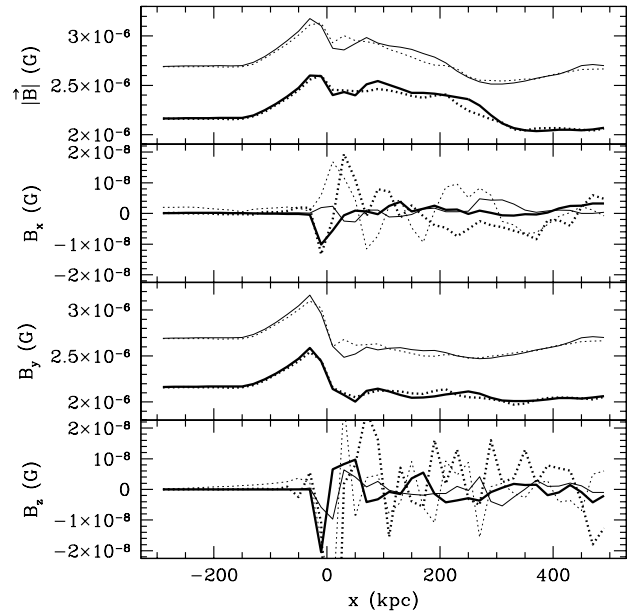


Figure A3. Mass-weighted average magnetic field magnitude, x , y , and z -components (from top to bottom) along x -axis for Case PP. The magnitudes are measured inside a cylinder of radius 120 kpc in radius at 5 Gyr. The original runs are shown as *thin lines* and the new runs for the strong ram pressure case as *thick lines*. The results are presented for Runs 0h (*solid line*) and 5h (*dotted line*). The bin size along x -axis is 20 kpc.

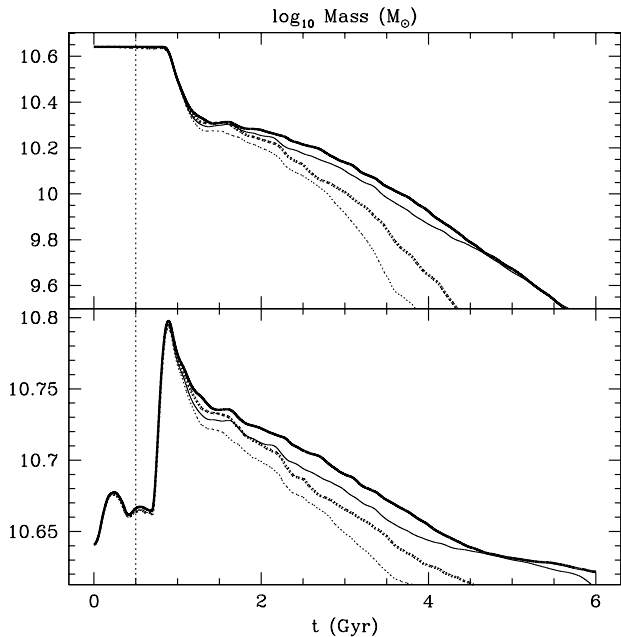


Figure A4. Mass evolution of the intrinsic ISM mass (*top*) and the total gas mass (*bottom*) inside R_t for the strong ram pressure in Case PP. With the exception of the vertical dotted line that corresponds to 0.5 Gyr when the ICM begins to flow into simulation box, all line styles have the same meaning as in A3.

run of Case PA are even larger than between Case PP and Case PA in the original runs, demonstrating that these differences in the total mass stripping rates can be attributed to the geometry of the field rather than its strength.

APPENDIX B: INITIAL MAGNETIC FIELDS IN THE STRONG RAM PRESSURE STRIPPING CASE

Figure 15 shows that the overall strength of the magnetic fields in Runs 0h and 5h of Case PP is larger than in Runs 0 and 5. The initial field strength in the ISM/ICM, as well as the strength of the field imposed at the inflow boundary, is the same in all of these runs. The difference in the strength of the evolved field is due to the fact that: (a) the field imposed at the boundary differs from that actually entering the computational domain (in the high ram pressure case the latter is slightly higher), and (b) the dynamical interaction of the inflowing ICM with the galaxy is different due to the different levels of ram pressure. In order to disentangle these two possible effects, we perform extra runs of strong ram pressure for Case PP in which we lower the initial field (and the field imposed at the boundary) to 1.15×10^{-6} Gauss. All other parameters are unchanged in these new runs. Upon entering the computational box, the field strength now approximately matches that in the original lower ram pressure run of Case PP.

We find that the general tendency to form a strong magnetic field layer in front of the galaxy is still present in the new runs. Figure A3 shows that a strong magnetic field layer forms around $x \sim -30$ kpc as in the original high ram pressure run. However, the strong ram pressure pushes the gas

with amplified magnetic field deeper into the galaxy than in the weak ram pressure stripping case, resulting in the amplification of the magnetic field over a wider range of distances. This conclusion agrees with our previous conclusion for the original high ram pressure run (see Figure 15).

Figure A4 presents the evolution of the intrinsic ISM mass and the total gas mass inside R_t in the new runs and original runs of Case PP. Decreasing the initial magnetic field strength reduces ability of the incoming ICM flow to strip the ISM in both Run 0h and 5h. This tendency is more pronounced in Run 5h than in Run 0h. This attenuated ISM loss is also consistent with the larger total gas mass in the galaxy.

The comparison of Figure A4 and Figure 14 confirms that the larger ISM mass loss observed in the strong ram pressure stripping case (i.e., Runs 0h and 5h) is indeed mainly determined by the velocity of the ICM inflow rather than the differences due to the dynamical effect of the magnetic field (i.e., rather than the different strength of magnetic fields in the inflowing ICM). Even after lowering the initial and boundary magnetic field strengths to ensure that the actual field entering the computational domain matches the field strength in the weak ram pressure stripping case, we find that the ISM loss in the strong ram pressure stripping case is far above that found in the weak ram pressure stripping case.